PL-TR-96-2248

DEVELOPMENT OF A COMPREHENSIVE HYDROACOUSTIC COVERAGE ASSESSMENT MODEL

Ted Farrell
Kevin LePage

BBN Systems and Technologies
1300 North 17th Street
Arlington, VA 22209

September 1996

Final Report
August 1995-August 1996

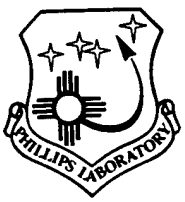

PHILLIPS LABORATORY
Directorate of Geophysics
AIR FORCE MATERIEL COMMAND
HANSCOM AFB, MA 01731-3010

DEPARTMENT OF ENERGY
OFFICE OF NON-PROLIFERATION AND
NATIONAL SECURITY
WASHINGTON, DC 20585

SPONSORED BY
Department of Energy
Office of Non-Proliferation and National Security

MONITORED BY
Phillips Laboratory
CONTRACT No. F19628-95-C-0174

The views and conclusions contained in this document are those of the authors and should not be interpreted as representing the official policies, either express or implied, of the Air Force or U.S. Government.

This technical report has been reviewed and is approved for publication.

DELAINE REITER
Contract Manager
Earth Sciences Division

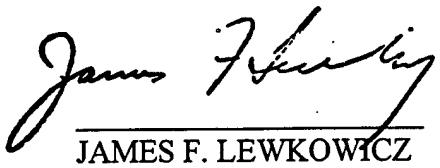

JAMES F. LEWKOWICZ
Director
Earth Sciences Division

This report has been reviewed by the ESD Public Affairs Office (PA) and is releasable to the National Technical Information Service (NTIS).

Qualified requestors may obtain copies from the Defense Technical Information Center. All others should apply to the National Technical Information Service.

If your address has changed, or you wish to be removed from the mailing list, or if the addressee is no longer employed by your organization, please notify PL/IM, 29 Randolph Road, Hanscom AFB, MA 01731-3010. This will assist us in maintaining a current mailing list.

Do not return copies of this report unless contractual obligations or notices on a specific document requires that it be returned.

DISCLAIMER NOTICE

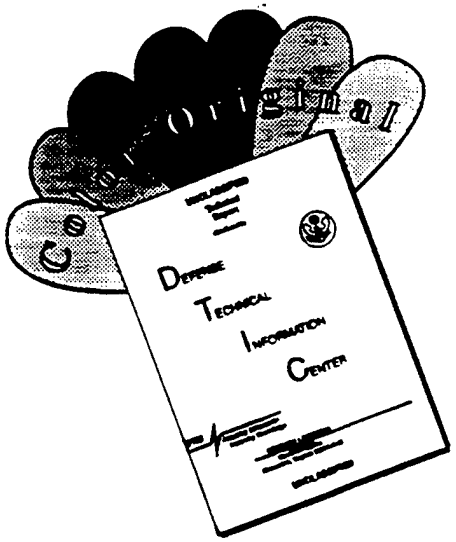

THIS DOCUMENT IS BEST QUALITY AVAILABLE. THE COPY FURNISHED TO DTIC CONTAINED A SIGNIFICANT NUMBER OF COLOR PAGES WHICH DO NOT REPRODUCE LEGIBLY ON BLACK AND WHITE MICROFICHE.

REPORT DOCUMENTATION PAGE

Form Approved
OMB No. 0704-0188

1. AGENCY USE ONLY *(Leave blank)*	2. REPORT DATE	3. REPORT TYPE AND DATES COVERED
	September 1996	Final Aug. 95 - Aug. 96

4. TITLE AND SUBTITLE

Development of a Comprehensive Hydroacoustic Coverage Assessment Model

5. FUNDING NUMBERS

Contract

F19628-95-C-0174

PE PR DENN TAGM WUAY

6. AUTHOR(S)

Ted Farrell and Kevin LePage

7. PERFORMING ORGANIZATION NAME(S) AND ADDRESS(ES)

BBN Systems & Technologies
1300 North 17th Street
Arlington, VA 22209

8. PERFORMING ORGANIZATION REPORT NUMBERS

Technical Memo W1278

9. SPONSORING / MONITORING AGENCY NAME(S) AND ADDRESS(ES)

Phillips Laboratory
29 Randolph Road
Hanscom AFB, MA 01731-3010

Contract Manager: Delaine Reiter/GPE

10. SPONSORING / MONITORING AGENCY REPORT NUMBER

PL-TR-96-2248

11. SUPPLEMENTARY NOTES

12a. DISTRIBUTION / AVAILABILITY STATEMENT

Approved for public release; distribution unlimited

12b. DISTRIBUTION CODE

13. ABSTRACT *(Maximum 200 words)*

A model for predicting the detection and localization performance of hydroacoustic monitoring networks has been developed. The model accounts for major factors affecting global-scale acoustic propagation in the ocean, such as horizontal refraction from bathymetric features and horizontal changes in sound speed, travel time variability due to spatial and temporal fluctuations in the ocean, and detailed characteristics of the source. In this report, a summary description of the component submodels, environmental databases and output products is provided. Several studies are presented which investigate the sensitivity of the predictions to the component sub-models and/or databases used. Travel time and travel time variance predictions are compared to measured data.

Finally, two example applications of the model are described; a prediction of the coverage of the International Monitoring System, and an analysis of the causes of a gap in the predicted coverage.

14. SUBJECT TERMS	15. NUMBER OF PAGES
hydroacoustics, localization, oceanography, performance prediction, test-ban verification	76
	16. PRICE CODE

17. SECURITY CLASSIFICATION	18. SECURITY CLASSIFICATION OF THIS PAGE	19. SECURITY CLASSIFICATION OF ABSTRACT	20. LIMITATION OF ABSTRACT
Unclassified	Unclassified	Unclassified	UL

NSN 7540-01-280-5500

Standard Form 298 (Rev. 2-89)
Prescribed by ANSI/NISO Std. Z39.18
298-102

Contents

Figures

TABLES

Acknowledgments

Several people have assisted in the development of HydroCAM through general discussions and by providing many of the base modeling capabilities contained in the model. In particular, Dr. Dave Harris at Lawrence Livermore National Laboratory (LLNL) has provided many hours of discussion and direction on the model requirements and practical aspects of collected hydroacoustic data from earthquakes and explosions. Dr. Delaine Reiter from the Phillips Laboratory provided oversight, administrative support and encouragement. Dr. Doug Clarke from Lawrence Livermore National Laboratory provided source starter fields from the CALE/NPE model. Dr. Ed McDonald of the Naval Research Laboratory (NRL) in Washington, DC kindly provided insight and feedback as the tool was developed. Dr. Greg Orris from NRL provided a copy of the G-SOAR horizontal raytrace software and discussed many of the design decisions that went into that model. Dr. Mike Collins at NRL provided the Range-Dependent Acoustic Model over the internet. The National Oceanographic and Atmospheric Administration (NOAA) and Woods Hole Oceanographic Institution (WHOI) provided the 3-D raytrace software HARPO which was evaluated during the initial stages of this effort. Dr. Mike Porter at the New Jersey Institute of Technology (NJIT) provided the Kraken normal mode model and an excellent set of documentation summarizing its development and use. Edward Scheer from WHOI graciously provided a summary of an ATOC experiment and travel time variance data from his web site. Dr. Greg Duckworth and Mr. Jim O'Connor of BBN have monitored the technical progress of this effort. We would also like to thank Dr. Jeff Angell of BBN for many hours of discussion and for reviewing the details of travel time variability models and localization area of uncertainty calculations.

1.0 Executive Summary

1.1 Introduction

Large amplitude underwater acoustic signals, such as those generated by earthquakes, volcanoes and explosions, can be monitored on a global-scale using a relatively small network of hydrophones. At the current time, the design and development of a system for monitoring compliance with a Comprehensive nuclear Test-Ban Treaty (CTBT) is underway. To assure that an effective monitoring capability is developed, a model that can predict the detection and localization performance of the network is required.

Although many acoustic performance prediction software packages are available, most of these programs were developed to predict the performance of active and passive SONAR systems for Anti-Submarine Warfare (ASW). Unfortunately, these "standard models" developed for ASW are not sufficient for CTBT purposes since (1) they usually neglect important properties of global-scale acoustic propagation such as horizontal refraction and (2) they do not provide estimates of travel time variability required to determine localization performance.

The Hydroacoustic Coverage Assessment Model (HydroCAM) was developed under funding of the U.S. Department of Energy (DOE) to predict the detection and localization performance of global hydroacoustic monitoring networks. It consists of oceanographic databases, acoustic propagation models, network performance models, and software for visualizing and interpreting results at each stage in the prediction process (See Figure 1). The model accounts for horizontal refraction from bathymetric features and geographic changes in sound speed, travel time variability due to spatial and temporal fluctuations in the ocean, and detailed characteristics of the source. HydroCAM's graphical user interface simplifies the process of setting up the models. Output products include maps of network detection coverage and localization area of uncertainty, as well as intermediate results such as predicted path amplitudes, travel time and travel time variance. Although much of the software is recently developed C++ code, existing models and databases developed by other institutions have been integrated where appropriate. The result is a flexible system with the ability to produce quick results, using simple geometric propagation models and low-resolution oceanographic databases, as well as the ability to produce results using research grade propagation models and high-resolution databases.

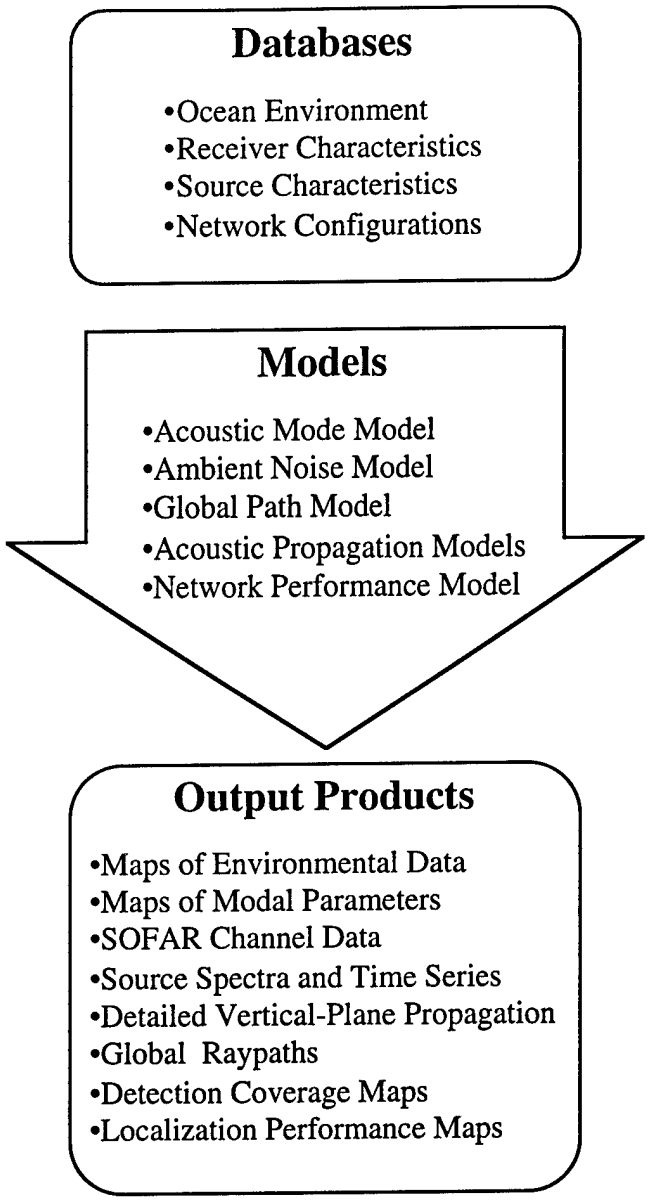

Figure 1: HydroCAM Components

1.2 Accomplishments

A number of products and services have been provided under this effort. A brief summary of these follows:

Developed model software and users guide -- HydroCAM was developed using an iterative build/test software design approach. Starting with the simplest reasonable

models for acoustic propagation, each module was prototyped and tested against measured data and more sophisticated models. Tradeoff studies were performed to determine the most appropriate submodels to include, based on the accuracy, sensitivity and processing time required for each model. HydroCAM itself was used to perform most of these studies, as well as model validation, beta-testing and example model applications. The functional details of HydroCAM were documented in a *Users Guide* [1]*. The example applications and tradeoff studies are the primary topic of this report. The list below summarizes the new software development that occurred under this contract:

- Developed C++ version of the NRL Global-Scale Acoustic Raytrace (G-SOAR)
- Developed C++ network detection and localization performance model
- Developed C++ ocean acoustic waveguide software
- Developed interfaces to the CALE/NPE hydrodynamic and non-linear propagation model for characterizing explosive sources
- Developed interfaces to Kraken and RAM "standard" linear propagation models
- Developed executive "shell" that integrates all models and databases
- Obtained and integrated the best available oceanographic databases

Provided beta-testing and training -- During the second week of May, a beta-version of software was delivered to scientists at the Lawrence Livermore National Laboratory (LLNL). On-site training was also provided. The purpose of this early delivery was to get feedback from the model users. Additional display formats and data output products were identified during this trip, and these products were incorporated into HydroCAM.

Delivered data and software to end-user community -- A prototype prediction program which estimates travel time using non-refracting (geodesic) ray paths and seasonal sound-channel databases was requested by both the Air Force Technical Applications Center (AFTAC) and Sandia National Laboratories (SNL). This prediction software, the necessary sound-channel databases, and a brief set of documentation were delivered to AFTAC in February, and SNL in April. Investigations early in the contract indicated that these models removed systematic biases in the previously used travel time model of up to 100 seconds. In July, travel time grids at 1 degree resolution for each of the hydroacoustic stations in the current International Monitoring System (IMS) were delivered to SNL. These grids are required for localization algorithms in any operational monitoring system, and will be incorporated into the hydroacoustic knowledge database.

Reported progress and results to the research community -- As required under the contract, BBN personnel attended both the 17th and 18th Annual Research Symposia on Monitoring a Comprehensive Test Ban Treaty. In addition, a program review was held in February where all interested parties provided feedback on the design of HydroCAM.

* Numbers appearing in brackets indicate references listed in Section 7.0

During the beta-delivery of the software at LLNL, a seminar describing the model capabilities and IMS performance predictions was given to scientists and engineers in the CTBT R&D Program. Finally, research results were presented at the 130th Conference of the Acoustical Society of America [2] and will soon be submitted as a journal article entitled "The effect of sound speed fluctuations on travel time variability and localization accuracy of global hydrophone networks" to the Journal of the Acoustical Society of America [3].

1.3 Major Results

Application of the HydroCAM model has produced the following conclusions relevant to hydroacoustic monitoring:

- The simplest reasonable propagation model must account for the ellipsoidal nature of the earth and the geographic and seasonal variations in the SOFAR channel sound speed. This model can accurately predict paths and travel times for large expanses of the ocean.

- The effects of horizontal refraction are required for cases where paths interact with bathymetric features such as continental shelves, islands and seamounts, and when paths traverse rapidly changing water temperature, such as the Antarctic convergence.

- The most efficient model for including horizontal refraction will likely use the WKB approximation for the calculation of the acoustic phase velocities, and a boundary value approach to finding refracted rays connecting two points.

- Travel time variance can be modeled reasonably well using the historical databases of sound channel fluctuations.

- Additional work needs to be done to confidently integrate source characteristics with long-range propagation models.

1.4 Summary

In summary, a comprehensive, user-friendly model has been developed to predict the ability of acoustic sensors to detect and localize nuclear explosions in and above the ocean. Predictions of the model have been compared against measured data. The model has been exercised by BBN and LLNL, and has been used to predict the performance of the IMS and to develop approximate travel time grids for SNL. In addition, a number of

studies have been performed to determine the sensitivity of the predictions to the models, interpolation techniques and/or databases used.

As previously stated, a complete description of the physics and use of the model is provided separately in the *HydroCAM Users Guide* [1]. The remainder of this report summarizes the tradeoff studies, model validation and model applications that have been performed. The report contains four major sections. First, the capabilities of the model are briefly described. The second section summarizes the studies completed using the model, which include sensitivity/tradeoff studies and some comparisons with measured data that were performed this year. Example applications of the model including the prediction of the capabilities of the IMS are presented. The report ends with a set of conclusions and recommendations.

2.0 Model Description

HydroCAM is a hydroacoustic network performance prediction program that runs on a UNIX workstation. It contains an assortment of oceanographic databases, acoustic propagation models, network performance models, and software for visualizing and interpreting results at each stage in the prediction process, as shown in Figure 2. Because we took advantage of the best existing models and databases, the components of HydroCAM are in a variety of data formats and software languages, from FORTRAN-77 to C++ and MATLAB. The graphical interface makes all of this transparent to the user, and provides a capability to perform these functions:

- Access, analyze, and display a variety of oceanographic databases.
- Create geographic databases containing acoustic modes and waveguide parameters.
- Predict global-scale acoustic propagation paths and their characteristics.
- Assess network detection coverage and localization performance.
- Include spatial and signal processing characteristics of acoustic receiver systems.
- Predict source effects on acoustic signals received at long ranges.

The following sections describe the functionality in each of these areas.

2.1 Environmental Databases

Compared to seismic propagation, characteristics of the worlds oceans are well known. In a sense, the US Navy, NOAA, and other oceanographic institutions have solved the "regionalization" problem for the worlds oceans. Oceanographic databases are available at a variety of temporal and spatial resolutions, from raw data to analyzed statistics, all in a wide variety of formats. The critical element is the ability to rapidly access, visualize, analyze and incorporate this data into propagation and network performance models. The databases included in HydroCAM are listed in Table 1. They contain information on environmental factors affecting low frequency ambient noise (shipping densities), high frequency ambient noise (ocean surface wind speed and rainfall), and acoustic propagation (sound speed profiles and bathymetry).

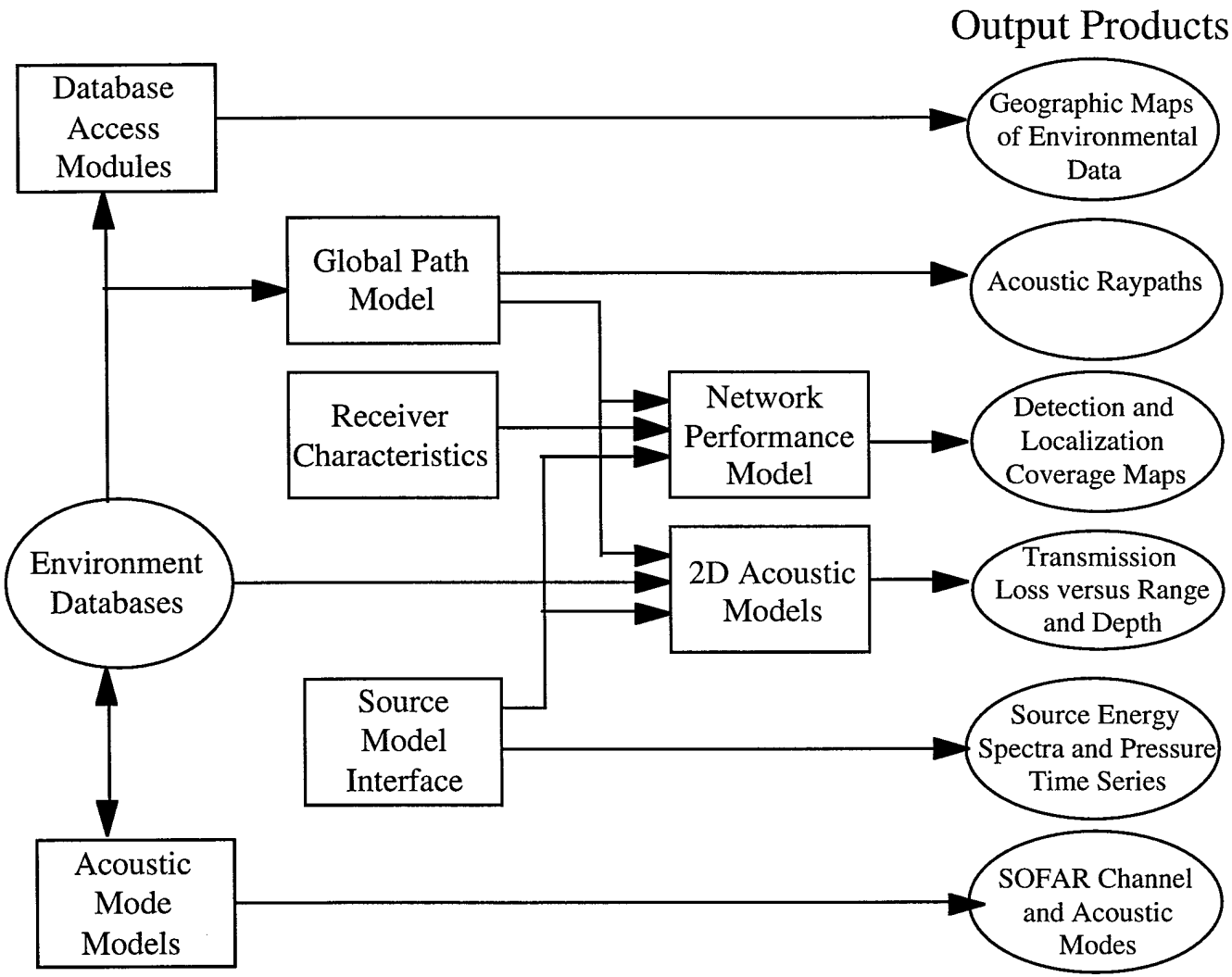

Figure 2: HydroCAM Components and Output Products

Table 1: Environmental Databases Included in HydroCAM

Database Name	Database Description	Temporal Resolution	Spatial Resolution (min)
ETOPO5	Bathymetry	N/A	5
GDEM	Sound speed profiles	Seasonal	30
WOA94	Temperature and Salinity	Monthly	30 and 300
HWS	Historical Wind Speed	Monthly	60
HITS	Historical Temporal Shipping	Monthly	Variable
GDS	Global Daily Summary (Temp/Precip)	Daily	Variable

HydroCAM allows users to interactively extract, visualize and analyze data for a given region with a graphical user interface. The left side of Figure 3 shows an example display containing bathymetry data for the South Indian Ocean. The small box in the center of the display was selected using a mouse. The locations of sound speed profiles from the WOA database that are available inside the boxed region are overlaid on the bathymetry. The plot on the right hand side of the figure shows the sound speed profiles. HydroCAM also enables predictions of the modal characteristics and acoustic propagation to be performed using this data without regard for the specific database format or the input formats required by the propagation model.

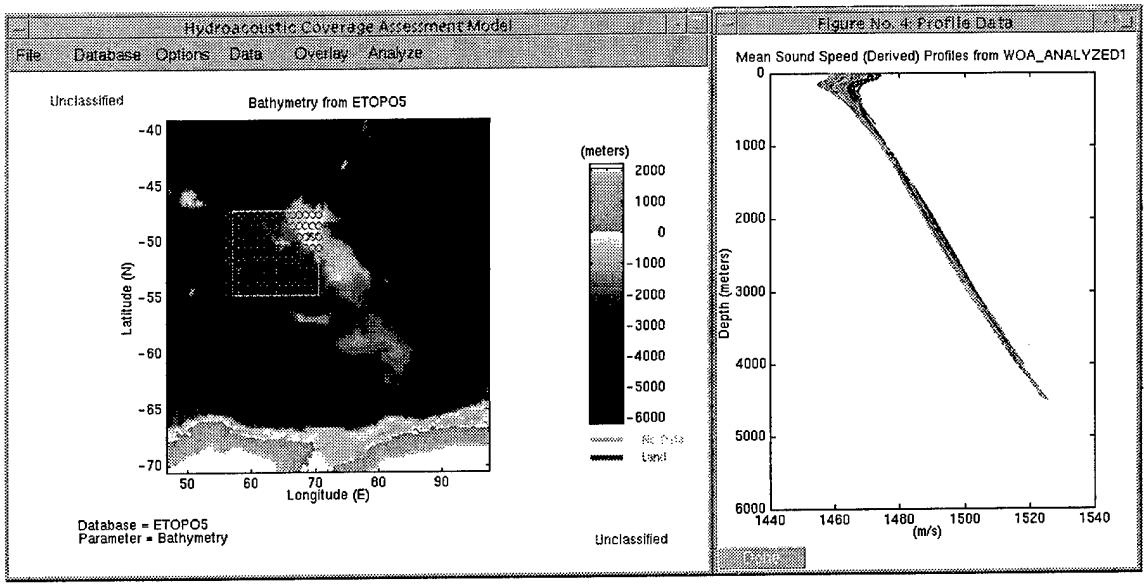

Figure 3: Example Display of Environmental Data

2.2 Ocean Waveguide Characterization

Two general options for characterizing the ocean waveguide are provided. The first assumes that all energy propagates in the SOFAR channel. In this case, the oceanographic characteristics at the SOFAR depth (which varies according to geographic location and season) are automatically extracted and provided to the propagation models. The second, more accurate, approach is to separate the vertical component of the problem by treating individual geographic locations in the ocean as range independent waveguides.

In this approach, the environmental data *at each location on a geographic grid* is used to calculate the mode structure in each of these "cells". Two models are available for computing the mode structure at each point; a well known normal mode code called Kraken from NJIT, and an approximation developed by BBN based on WKB theory. Kraken calculates exact eigenvalues for as many modes as are necessary locally, while the WKB code rapidly calculates approximate eigenvalues for only those modes requested. Since it is expected that received signals will contain energy from the first several modes only, the WKB should result in a significant time savings. After the mode structure has been determined, the local phase speed, group speed, modal attenuation and slowness variance [1] are computed. The results are placed into four geographic grids, which are provided as inputs to the propagation models. Figure 4 shows an example display of a group speed grid at 10 Hz, calculated using annual average sound speed profiles and the Kraken model at each of 36705 geographic locations. To produce these "derived databases" involves extracting environmental data from a diverse set of databases and running a set of software packages on tens of thousands of geographic locations, a task that was previously required manual intervention at many intermediate steps. With the new software interfaces, thousands of model runs and management of the data has been automated. New environmental databases that include seasonal fluctuations and new data collected in the Southern Hemisphere have also been integrated, resulting in the ability to produce better knowledge grids of the ocean characteristics with significantly less effort.

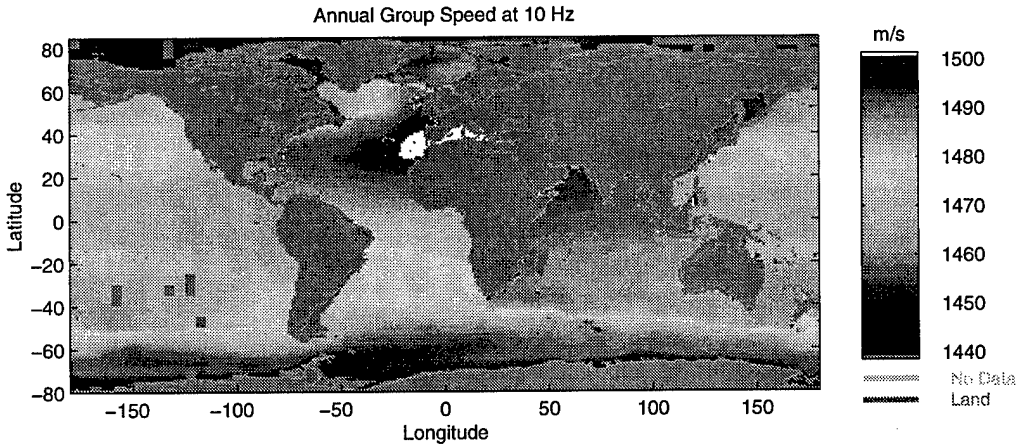

Figure 4 :Calculated group speeds at 10 Hz for the worlds oceans.

2.3 Propagation Path Predictions

Acoustic paths are calculated in 2 steps. First, the path itself is calculated, then the travel time, travel time variance and amplitude are calculated along the path. The five candidate path models that were evaluated are: (1) a geometric path model on a spherical earth for reference, (2) an ellipsoid (geodesic) model, (3) the horizontal ray/vertical mode model developed by NRL, (4) a bender model, and (5) the 3-D raytrace program HARPO. Studies early in the effort comparing predicted travel times using spherical paths and ellipsoid paths to measured travel times from the September 1995 French nuclear tests resulted in the elimination of the spherical model. The 3-D raytrace model was also eliminated after acceptable travel time predictions were obtained using the other models with significantly less computational load. The remaining models are part of the baseline capability of HydroCAM. Once raypaths are calculated, the travel time, amplitude and travel time variance along each path are calculated by performing path integrals of the appropriate grid database quantity along the path. For example, travel times are calculated by integrating the inverse of the group speed along the predicted path.

Output products at this stage include plots of the paths and their characteristics. If the predictions are run from a receiver to a grid of sources (eigenray mode), plots of the path data at the endpoints on the grid are produced. These grids are used to determine network performance as described in Section 2.4. The grids are also used to investigate the ray stability and the sensitivity of predicted travel times, amplitudes, modal content and horizontal multi-path to environmental variability and database interpolation.

The option for extracting sound speed profiles and bathymetry in a vertical plane along the path is often used to investigate blockage. In addition, this environmental information can be passed on to "standard" vertical plane propagation models such as the Range-dependent Acoustic Model (RAM) developed by NRL. This capability is used for determining detailed propagation characteristics along the paths, effects of bathymetric features on loss mechanisms and mode structure, and the detailed structure of the arrival from a specified source. Figure 5 shows examples of some of the data products produced by the path model. The output products illustrated include (a) locations of the acoustic paths from a receiver at Ascension Island, (b) travel time along these paths, (c) sound speed and bathymetry along one of the paths in (a) ending near Australia, and (d) transmission loss in a vertical plane along the path used in (c).

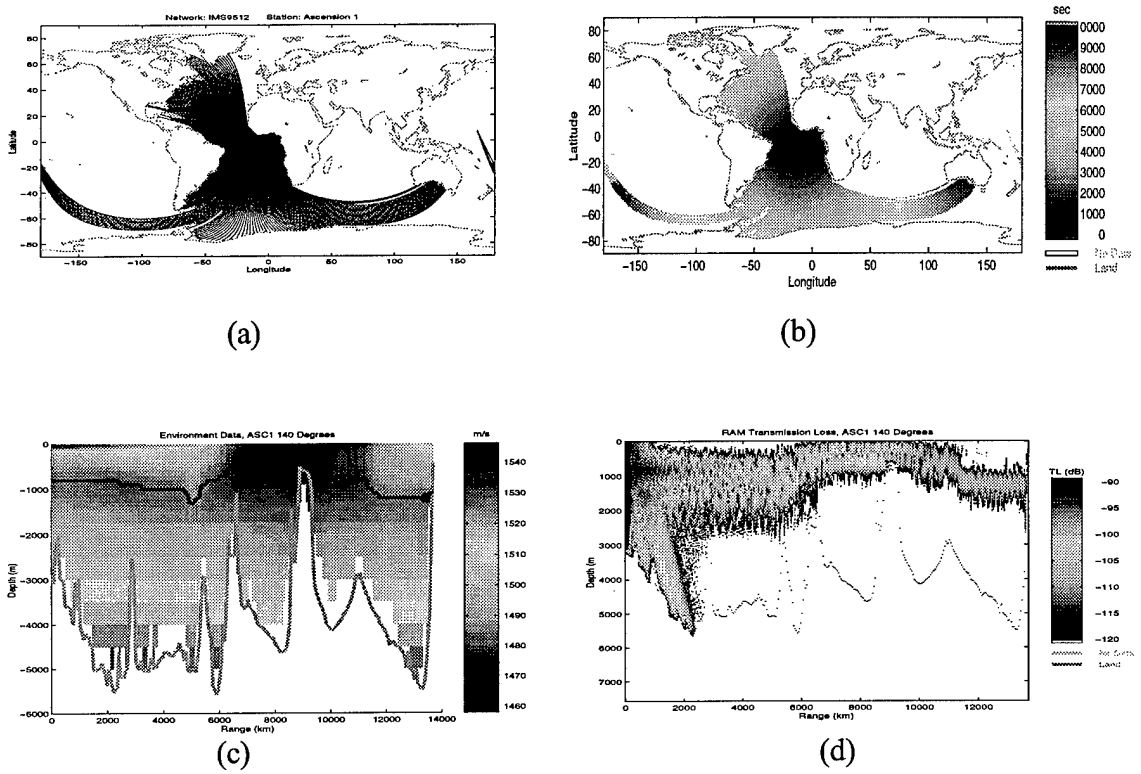

Figure 5:Example output products of the path model : (a) paths, (b) travel time, (c) sound speed and bathymetry, (d) propagation loss

2.4 Network Performance Evaluation

The performance of a network is described in terms of the ability to detect and locate sources. The detection performance of a single sensor is measured by the signal to noise ratio (SNR) observed at the sensor output. SNR is usually defined as the peak value of the receiver output relative to the background noise or interference level, and may be calculated for a complete event, or for a single component phase. It can be related to a number of other performance metrics, such as detection probability and arrival time accuracy. However, transformation into detection probability requires a model for the receiver output statistics and specification of a detection threshold. Since these are usually determined empirically, we have opted to produce SNR only.

Single-receiver SNR may be used to display the detection coverage or combined with SNR estimates for receivers at other locations to compute the performance of the hydroacoustic network as a whole. Many SNR-related data products are available, including geographic plots of:

- SNR for a specific receiver, corresponding to different event locations (for evaluation of existing assets)
- SNR for a specific event location, yield and depth/height for various receiver locations (for evaluation of alternative locations for new sensors).
- The minimum SNR seen by all receivers in the network
- The Mth largest SNR value seen by the network
- The number of receivers receiving the event above a specified SNR threshold. This plot is particularly useful for interpreting localization solutions.

The metric for localization coverage is area of uncertainty (AOU), which summarizes the effect of all the uncertainties in the localization calculation, including model uncertainties, e.g., uncertainties in the assumed propagation speeds. At the current time, the AOU model is based on localization using arrival time of one specific phase at multiple receivers. Additional measurements, such as bearing, can be readily added to the algorithms. The size of the AOU is a function of the accuracy of the travel time model, the ability to correctly measure the arrival time of the modeled phase, and the sensor-event geometry. This effort focused on modeling the effects of sensor geometry and the travel time model. Uncertainties in propagation speeds are included in the travel time variance calculations of the path model, using world-wide statistics of the sound speed derived from the WOA94 database and a sophisticated model for the slowness variance of propagating modes [1] . Measurement uncertainties, which depend on SNR and the specific signal shape are currently modeled parametrically, as an independent "picking" error added to the travel time error. Measurement uncertainties and the biases due to horizontal refraction will be investigated in the future. The primary output products of the localization model are geographic plots of the AOU and specialized display formats showing contributing receivers and path characteristics for a particular source location. Figure 6 shows an example AOU prediction for the IMS network. Sources were placed at every location on a 1 degree by 1 degree grid. This example includes the travel time variances using historical statistics of the ocean sound speed, but ignores the effects of horizontal refraction.

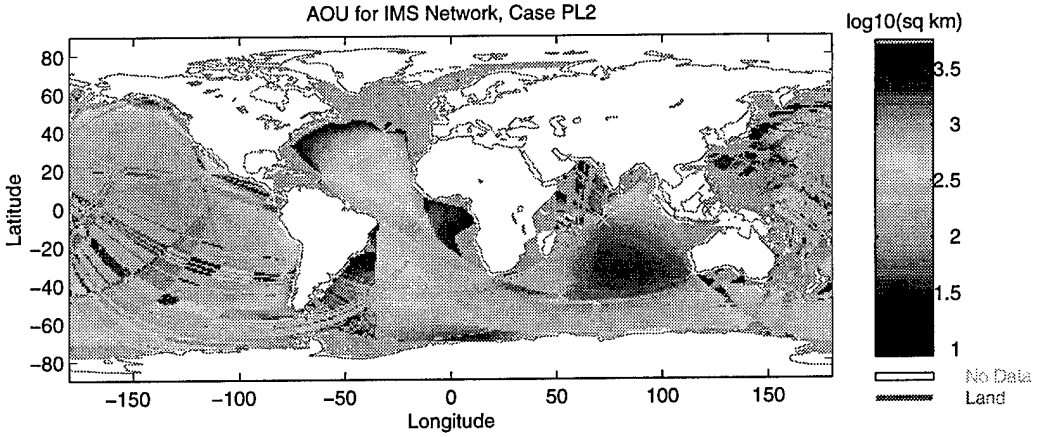

Figure 6: Example output product from the network performance model.

2.5 Source Effects

The performance of the network and the details of the arrival structure depend on the characteristics of the source. DOE funded research at LLNL and NRL has produced a combined hydrodynamic and non-linear acoustic model of the pressure signature from underwater and low-atmosphere nuclear bursts called CALE/NPE [4]. The principal development effort for the source portion of HydroCAM was to couple the source functions produced by this model to the linear acoustic propagation models contained in HydroCAM. Standard models that predict the pressure signature of low-level conventional explosions are also being investigated [5].

The source function is provided as pressure time series vs depth at a range where the acoustic propagation becomes linear (typically about 10 km from the burst). HydroCAM reads these files and calculates the complex pressure and the Energy Source Level (ESL) over a cylindrical surface in the water column as a function of depth and frequency. This data is used as a "starter field" for the linear propagation model: that is, the complex pressure is the input to a range dependent propagation model which estimates the complex propagation transfer function, and hence transmission loss (TL) at multiple frequencies along selected bearings from the event position. The result is the estimated received spectral level, for each frequency, to any selected range and depth along these radials.

Output products include displays of the source time series, spectral characteristics and ESL. Figure 7 shows some examples. In addition, plots of the received energy in a vertical plane along any geographic path can be produced, as illustrated in Figure 8.

There are many uses for these products, including investigation of potential evasion scenarios, and potential discrimination methods. As an example, the pressure signatures calculated by CALE/NPE contain the most important physical characteristics of underwater and atmospheric explosions. When coupled with the long-range models provided in HydroCAM, the predicted spectral characteristics of the received waveforms may provide important discrimination/estimation clues. In addition, the effects of different environmental conditions in the vicinity of the source, such as bursts on a continental shelf, can be investigated.

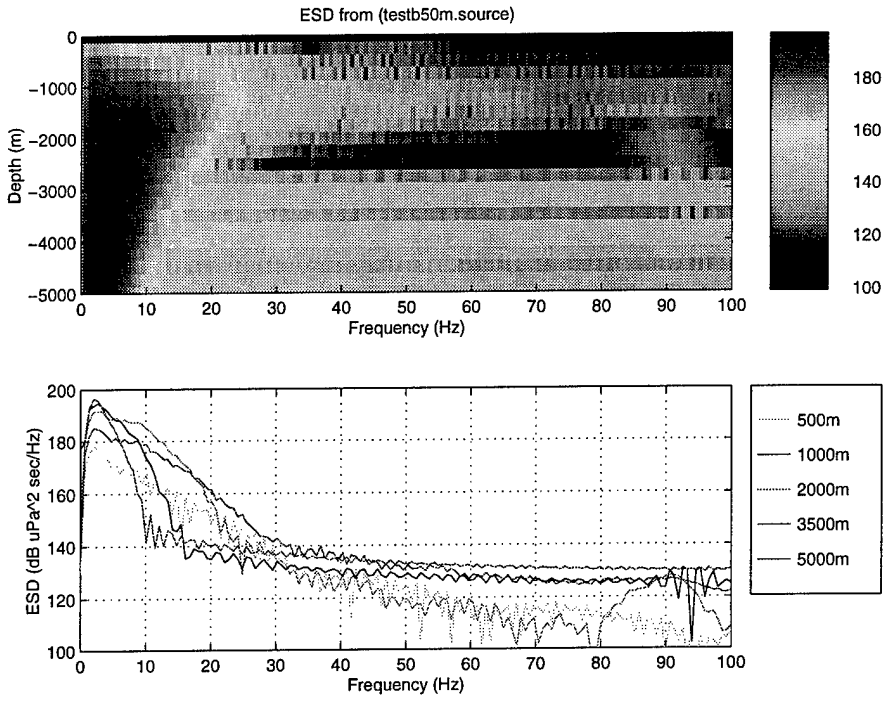

(a)

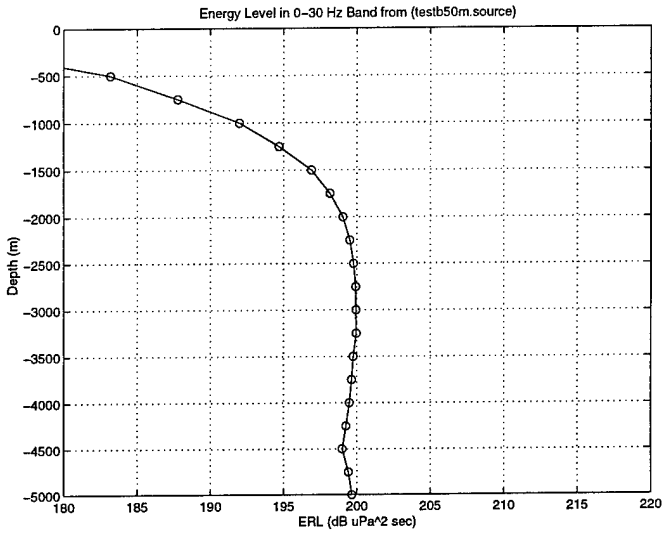

(b)

Figure 7: Example Source Displays: (a) Energy Spectral Density of 1kT explosion predicted by CALE/NPE Model, (b) Energy Level in 1-30 Hz Band

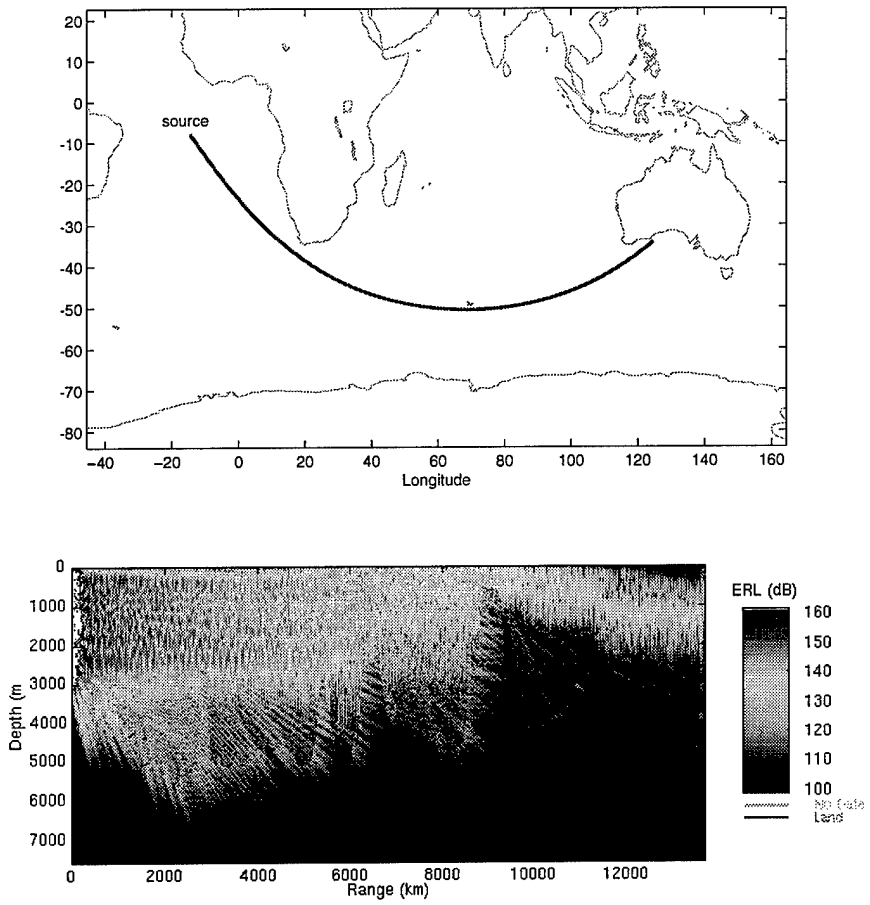

Figure 8: Energy level at 20 Hz calculated by RAM using a starter field for a 1 kT explosion at 50m calculated by CALE/NPE. (The path is illustrated at the top).

2.6 Receiver Characteristics

The primary receiver characteristics that affect network performance are the ambient noise background at the sensor location, the transfer function of the sensors, and the characteristics of any spatial and/or temporal processing. Ocean ambient noise over most of the frequency range of concern, 1-200 Hz, is principally due to distant shipping, resulting in a receiver noise field concentrated near the horizontal which varies in both azimuth and frequency. HydroCAM accounts for ambient noise using a table of noise level vs frequency and azimuth for each station in the network. These tables can be produced from measured data at the location if available, otherwise standard underwater noise models, such as the Wenz model [6] are used.

Some stations may have different sensor capabilities. For example, the island seismic stations in the proposed IMS are likely be on the order of 40 dB less sensitive than

hydrophones placed directly in the SOFAR channel [7]. These effects, along with additional losses due to hydrophone sensitivity, scalloping loss, or any other system SNR losses are accounted for in a loss table vs frequency. "Picking errors" are characterized by an arrival time variance term for each station, which is added to the travel time variance calculated by the path model. Typical values are 5 seconds for island seismic stations and 1 second for hydroacoustic stations [7].

In general, acoustic receivers can range in complexity from single omnidirectional hydrophones to arrays of hydrophones in various configurations. The spatial processing advantage produced by an array is measured by its array gain, which is proportional to the level of a beam output relative to an omniphone. In other situations where single hydrophones are located close to bathymetric features, it may be more convenient to model the effect of the feature as a directionality inherent in the sensor. In HydroCAM, the spatial characteristics of the receiver in both of these cases are specified either by a table of noise level versus azimuth and frequency, which represents the beam output in each direction, or by a table of array gains vs frequency and azimuth, which is applied onto the omnidirectional noise table described above. Array gains must be calculated offline using the location and orientation of the array and the beamforming parameters, such as spatial shading functions, number of beams formed, and pointing directions.

3.0 Sensitivity and Tradeoff Studies

In addition to the ability to predict network performance, the important new features in HydroCAM, which are not available in either the "Standard ASW" models or the NRL research model, are the combined (1) ability to include horizontal refraction and seasonal oceanographic databases, (2) the ability to predict travel time standard deviation, and (3) the ability to include source effects. As these features are non-standard, they were the focus of our sensitivity and tradeoff studies.

3.1 Travel Time

Since localization is one of the priorities for the hydroacoustic component of the monitoring system and no standard model exists for predicting the travel time on global scales, travel time was a major focus of the development effort for HydroCAM. Research published in JASA [8] has shown that for nearly antipodal paths which traverse the Antarctic convergence, a model which includes horizontal refraction (HR) with the vertical structure calculated using normal modes, was required to successfully predict travel times. However, the use of HR and normal modes comes at a high computational cost. As an example, using the geodesic/SOFAR channel model to compute travel time on a 5 degree grid encompassing the Indian Ocean takes approximately 5 minutes on a SPARC20 workstation, but the equivalent calculation using bisection applied to horizontal refraction can take 4 hours. The corresponding calculations required to develop the phase speed grids can take days.

Since the test case in [8] was for propagation to the vicinity of an antipode (a stressful case), it was decided to determine if there were other situations where HR was not required and a simpler, less computationally intensive approach would suffice. It was further decided to investigate the WKB approximation for calculating the modal parameters to speed up the normal mode calculations.

Finally, it is important to note that the standard approaches for finding raypaths that connect known source and receiver locations (eigenrays) result in long search times and/or instabilities of the initial value approach to solving the eigenray problem. An alternate approach was built into HydroCAM, which uses the so-called bending method, in order to investigate these issues.

The issues which were addressed in the travel time studies therefore included:

- Under what circumstances does HR need to be accounted for ?
- How simple a model can be used when HR is not necessary ?
- How sensitive are the results to database uncertainties ?

- How sensitive are the results to database interpolation methods ?
- What is the effect of using approximate modal values ?
- Do alternative boundary-value approaches to finding eigenrays show promise for global-scale problems ?

The descriptions that follow start with the simplest baseline possible, and determine the sensitivities and biases of this baseline model with respect to increasingly sophisticated models. In other words, an attempt is made to find the simplest model that works for some realistic scenarios, rather than start with the most complicated model. During these studies, the predictions were also compared with measured data (see Section 4.0). For context, assume that the desired localization accuracy is on the order of 1000 km^2. In this case, travel time uncertainties on the order of 20 seconds or less are certainly important. The starting assumption is that the simplest feasible model is a spherical earth with a constant sound channel speed.

3.1.1 Channel Sound Speed

The first study compares the travel time predicted using an ellipsoidal earth and a single constant sound speed to an ellipsoidal earth where the sound speed changes geographically (using the annual average of the SOFAR velocity at each geographic location). The sound speed at shallow depths is driven primarily by the ocean temperature. This causes sound speed profiles, and the SOFAR channel depth, to change geographically, especially at high-latitudes (See Figure 9).

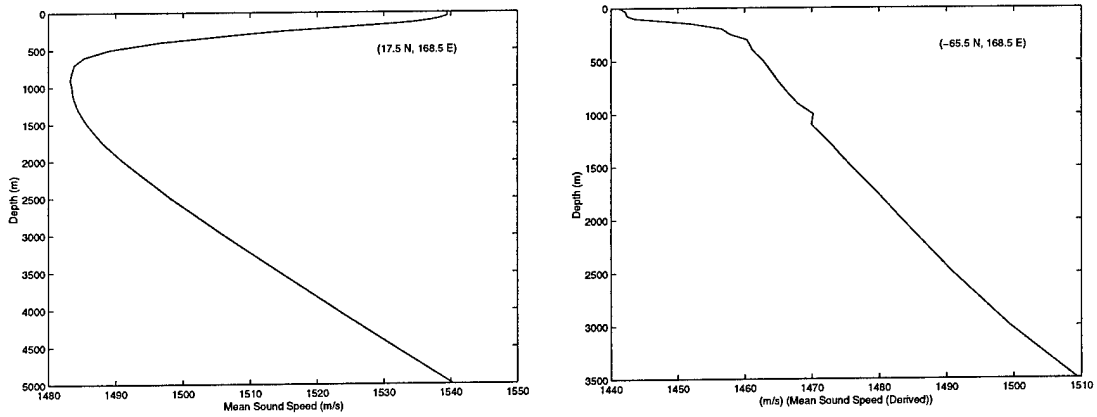

Figure 9: Mid-Latitude (left) and High-Latitude (right) Sound Speed Profiles

The SOFAR velocities were computed by finding the minimum of each sound speed profile in the World Ocean Atlas (WOA) database, which has a 1 degree resolution. Bilinear interpolation was used at each point spaced 10 km along geometric paths from a receiver near Ascension Island to a grid of source locations. The travel times were then calculated by trapezoidal integration of

$$t_{slow} = \int_S \frac{ds}{c(s)}$$

The result, shown in Figure 10, indicates that biases on the order of 100 seconds are present, with the greatest differences occurring when the paths go through areas that deviate from the constant sound speed.

3.1.2 Geodesic Earth Model

The second study compares the effect of a ellipsoidal earth model to the spherical earth model. Travel times were computed as described above using the annual average SOFAR channel sound speeds. The results shown in Figure 11 indicate that the difference in predicted travel times can be up to 20 seconds, with the largest errors occurring in locations to the due north and due south of the receiver location. These errors were also evident in comparisons with measured arrival time data from the 1995 French nuclear tests in the South Pacific, where the geodesic predictions were within 1.5 seconds of the measured value and the spherical earth predictions were 23 seconds off the measured value (see Section 4.0 for more details on model/data comparisons).

3.1.3 Seasonal Databases

As mentioned above, the sound speed at shallow depths is driven primarily by the ocean temperature. This causes sound speed profiles to change markedly in structure as a function of season. Travel times were predicted from a receiver near Ascension Island to a set of grid cells using each of 12 monthly sound channel values derived from the WOA database. The minimum and maximum travel time at each geographic location was saved, and the difference computed as shown in Figure 12. The results indicate that, as expected, the maximum deviations occur in paths which sample high-latitude waters near Antarctica, with differences as great as 25 seconds for paths with travel on the order of 2000 km.

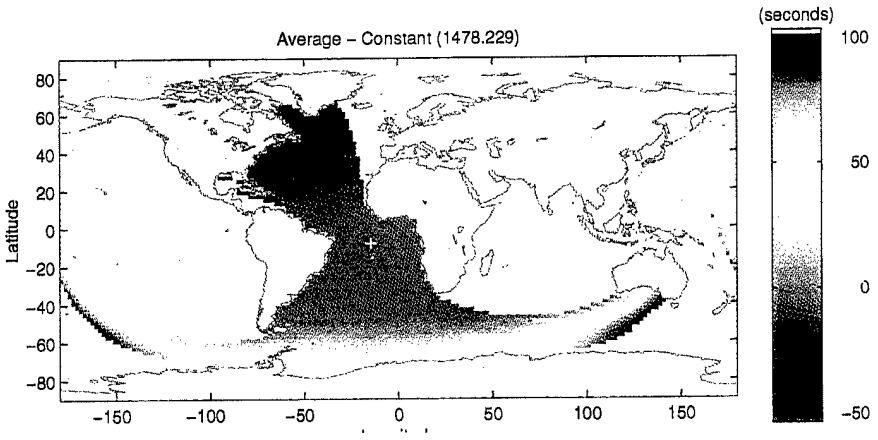

Figure 10: Difference between predicted travel time using constant sound speed and average SOFAR channel sound speed along geodesic paths

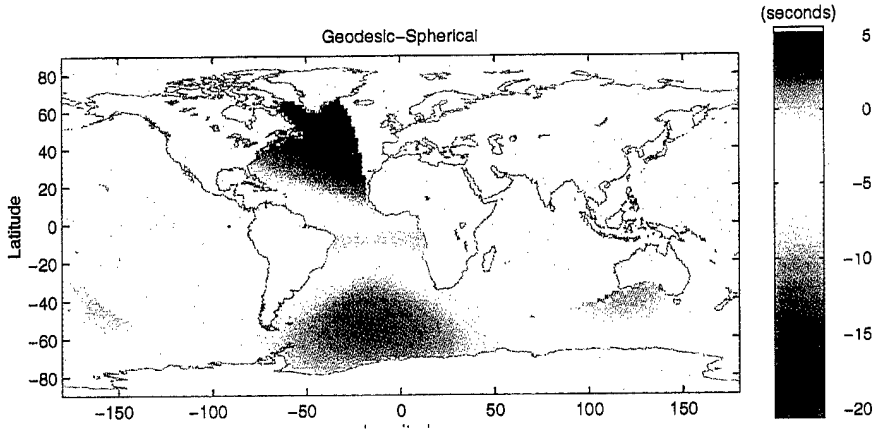

Figure 11: Difference between predicted travel time using ellipsoid and spherical earth

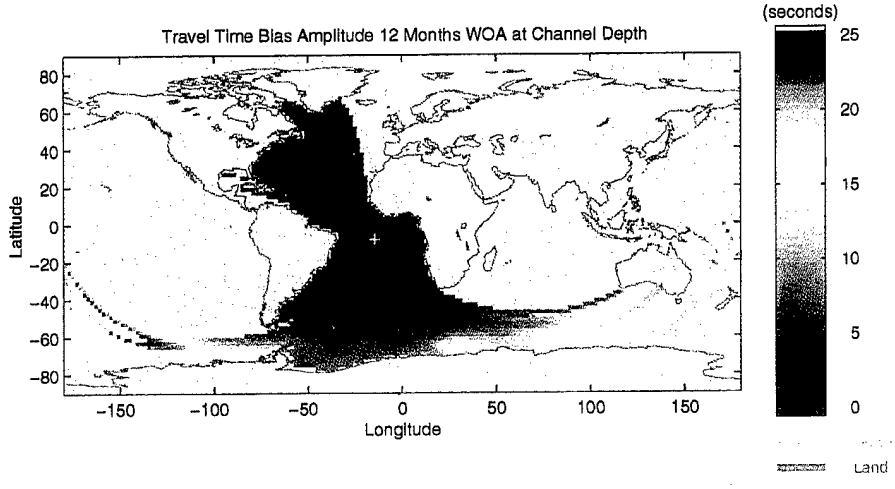

Figure 12: Maximum difference between travel time predicted using monthly sound-channel speeds and annual average sound-channel speeds

3.1.4 Horizontal Refraction

Previous studies have shown that horizontal refraction is required to adequately predict travel time in antipodal cases [8]. However, comparisons between predictions and data for less stressful cases (see Section 4.0) indicate that there are many situations when horizontal refraction is not required. To estimate the magnitude of horizontal refraction effects on travel time bias and blockage, we predicted paths from the Cape Leeuwin receiver in the Indian Ocean with and without horizontal refraction.

In the first test, eigenrays were predicted from the Cape Leeuwin receiver to a set of source locations on a 5 degree geographic grid. Figure 13 shows the difference between the refracted and geodesic travel times indicating that a travel time bias of up to 10 seconds can be produced. Although this effect is significant, it is our opinion that the primary reason we need to include horizontal refraction is to accurately predict coverage, as is shown in the second test case.

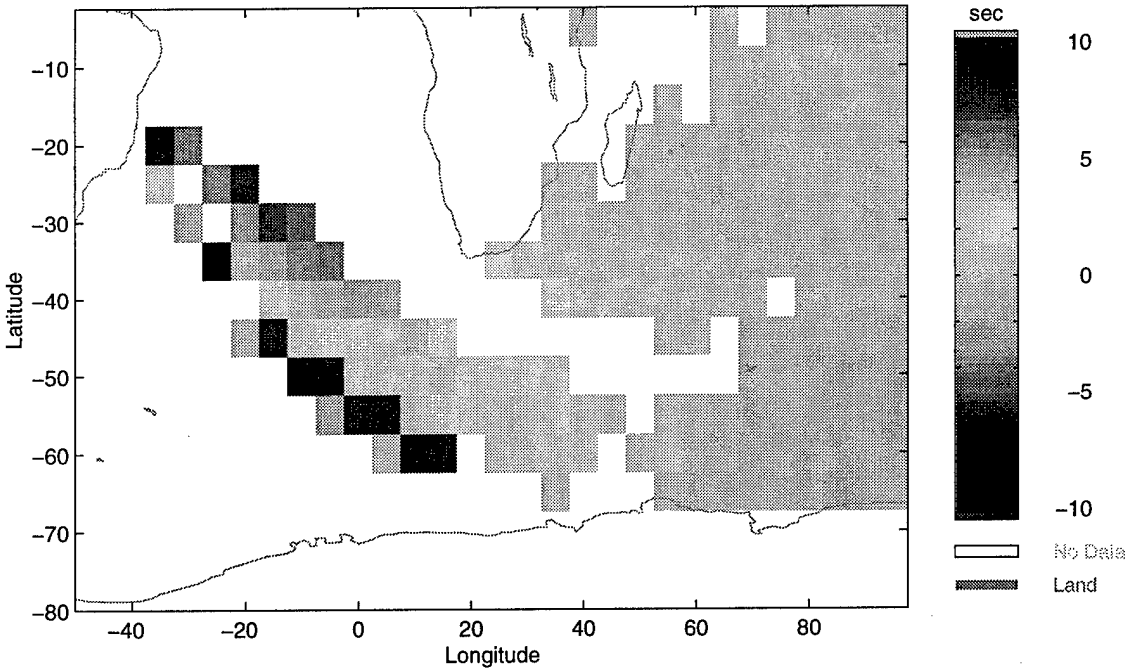

Figure 13: Travel time bias in South Indian Ocean due to horizontal refraction

In the second test, paths were determined by shooting rays from 220 to 240 degrees true north at increments of 0.1 degrees. For the horizontally refracted prediction, a phase speed grid at 0.5 degree resolution was used for the entire ocean. Two high-resolution (0.1 degree) phase speed grids were used at Kerguelen and Crozet Islands. All of the phase speed grids were calculated using the WKB model for mode 1 at 10 Hz. Figure 14 shows that the geodesic ray paths produce a markedly different shadow zone behind Kerguelen Island.

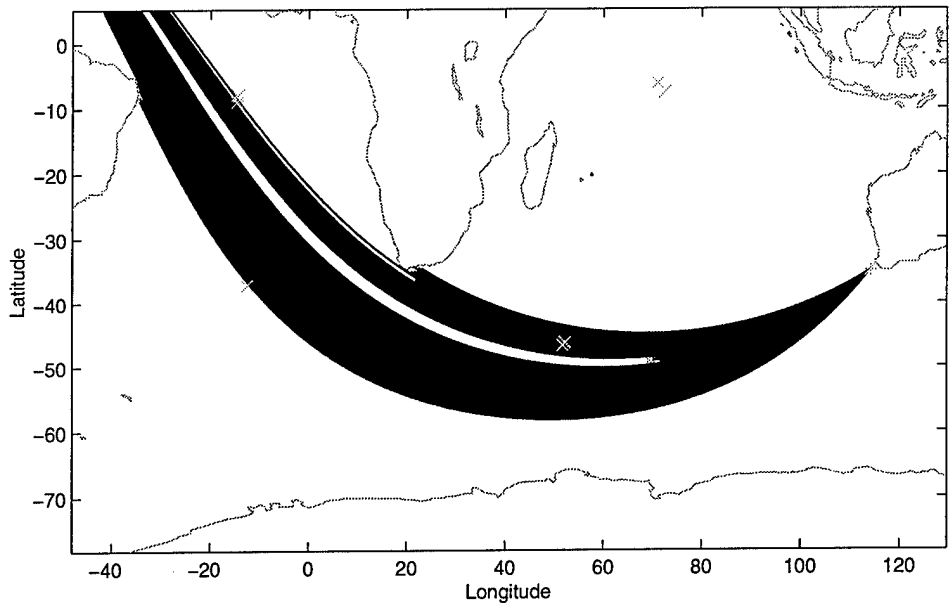

(a)

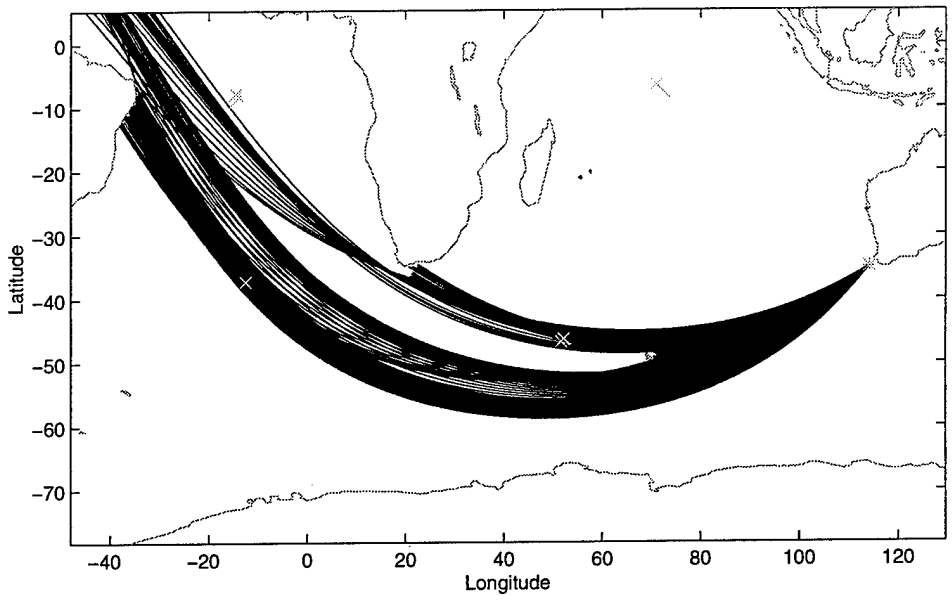

(b)

Figure 14: Blockage behind Kerguelen Island (a) using geometric paths and (b) including the effects horizontal refraction for mode 1 at 10 Hz

3.1.5 Three-Dimensional Ray Trace

At the beginning of the study, HARPO, a three-dimensional raytrace program, was obtained from NOAA/WHOI. This program solves the ray equations in spherical coordinates [9]. The purpose was to evaluate any advantages that this model might have over the combined modal/raytrace approach taken by NRL. This model was integrated with the environmental databases, and test cases were run from the Heard Island Feasibility Test (HIFT) source site to Ascension Island. A single ray trace from this source over the 9000 km path took over 5 hours running on a SPARC20 workstation. An analysis of the runs indicated that 75 percent of the computational load was interpolating the sound speed profiles, and that it would be possible to significantly speed up this portion of the computations. However, this model would put even greater computational constraints on network performance predictions since the test case did not search for a connecting raypaths. In addition, HARPO in its present form uses a spherical earth model (which was shown inadequate in the studies above), and does not include amplitude calculations. For these reasons, HARPO was not included in the remaining development of HydroCAM.

3.1.6 Modal Parameters vs Channel Sound Speed

Previous attempts by Munk *et al.* [10] to model the Perth-Bermuda path with an ellipsoidal earth and horizontal refraction produced a shadow zone that included the Bermuda receiving station. In the NRL paper referenced above [8], Heaney *et al.* successfully argued that the reason for this failure was the use of the SOFAR channel sound speed instead of the local phase speed. However, the use of phase speeds greatly increases the amount of computation required, since the normal mode problem must be solved at each geographic location on a global grid, and at each location in higher-resolution grids near areas containing significant bathymetric features. In addition, the use of normal modes brings the frequency and mode number parameters into the problem, which otherwise can be ignored when the channel sound speed is used. It is well known that the Perth-Bermuda path is nearly antipodal, which results in a number of extreme sensitivities that may not be present in other cases. A reasonable concern is whether use of the phase speed is required in other situations.

In this section the differences in raytraces using the channel sound speed versus the phase speed calculated using the Kraken normal mode model at 10 Hz are investigated. The WOA annual sound speed database was used for these calculations. Figure 15 shows the difference between the phase speed and the channel sound speed for this situation. Note that the phase speed is higher at high latitudes since channel ray paths (or modes) sample higher sound speeds at these latitudes. (See Figure 9 for a comparison of sound speed profiles at different latitudes). This suggests that the largest differences between rays

traced with the channel sound speed and rays traced using the phase speed will occur when paths traverse high-latitude waters.

In Figure 16 raypaths computed from Wake Island at launch angles every 10 degrees from 0 to 360 degrees are illustrated The figure shows that in addition to the large differences seen in paths traversing near Antarctica (see the paths in the South Atlantic Ocean), there are significant differences near bathymetric features, such as Hawaii. These differences occur since the phase velocity increases as water depth decreases.

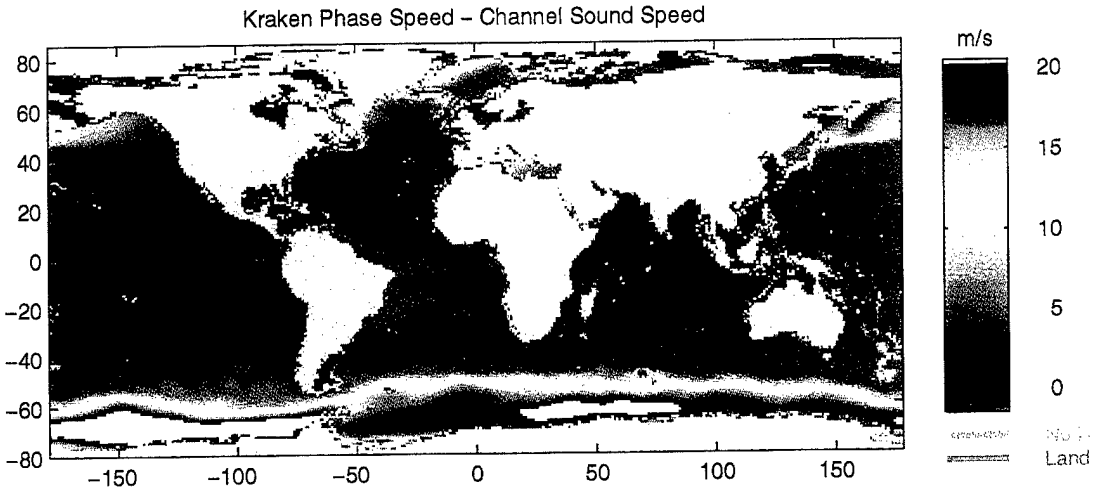

Figure 15: Phase speed for mode 1 at 10 Hz versus Channel Sound Speed

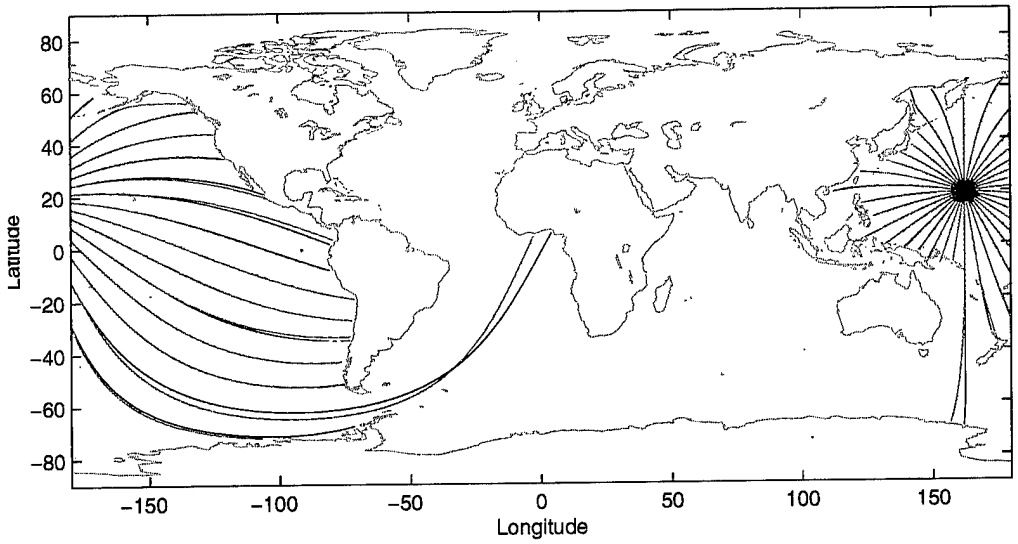

Figure 16: Raypaths traced from Wake Island receiver using (blue) Kraken phase speed grid at 10 Hz, and (red) channel sound speeds from the WOA database

3.1.7 WKB Approximation

Since the modal structure is required at each geographic location in a world-wide grid, a modest time savings in the modal computations at a single location translates into a large time savings when calculating a global grid. A second mode model provided in HydroCAM attempts to provide a faster but more approximate calculation of the mode structure by employing the Wenzel-Kramers-Brillouin (WKB) approximation. It has the additional benefit of calculating only the desired modes. It is a hybrid WKB Finite Difference (FD-WKB) approach which estimates the modal eigenvalues using the WKB approximation, and then calculates the mode shapes and refines the eigenvalue estimates using finite-differences. This technique is faster than Kraken, which is also a FD formulation, because the eigenvalue estimate obtained with the WKB approximation is much more quickly obtained than determining the eigenvalue directly from the FD matrix. Kraken is also slowed by the fact that it returns all the mode shape functions and eigenvalues which fall between the user supplied phase velocity limits. In interactive global propagation studies, often only one mode at a time is required.

The details of the WKB-FD method are provided in Appendix A of the HydroCAM Users Guide [1]. Here we compare global grids of the phase speed between Kraken and WKB. The phase speed v_n is a function of the modal eigenvalue k_n and the frequency ω

$$v_n = \frac{\omega}{k_n}.$$

The accuracy of the phase speed computation is of primary importance since (a) the phase speed gradient determines where the ray paths go, and (b) the phase speed could be used in the future to estimate the group speed using finite differences. The current calculation of the group speed in HydroCAM is performed by numerically integrating an expression derived using perturbation theory [1]. The modal group speed u_n, or its reciprocal the modal slowness S_n, is the major factor in determining the travel time along a path. The equation for the modal slowness is a function of the mode shape function $\psi(z)$, the density $\rho(z)$, and the sound speed profile $c(z)$

$$S_{gn} = \frac{1}{u_n} = \frac{dk_n}{d\omega} = \frac{\omega}{k_n}\int_0^D \frac{\psi_n^{\,2}(z)}{\rho(z)c^2(z)}dz,$$

where z is the depth variable and D is the depth of the acoustic bottom. If it is determined that the WKB method accurately estimates the phase speed, then further speed ups may be possible by eliminating the numeric integration in the above equation and instead using the WKB phase speed at adjacent frequencies to approximate the derivative.

Figure 17 shows the difference between the Kraken computed phase speed for mode 1 at 10 Hz and the WKB approximation. The WKB calculations, which were performed on a 1 degree global grid, took approximately 1/2 hour on a SPARC20 workstation. The Kraken calculations for the same grid took over 5 hours. The approximation is shown to be less than 0.2 m/s from the Kraken value over large regions of the ocean surface. In fact, the cumulative distribution of the errors, shown in Figure 18, indicates that 90% of the cells are approximated to within 0.3 m/s. These results show that the WKB is promising, but the issue of the accuracy of the phase speed gradients, and more importantly, the locations of the resulting ray paths needs to be addressed.

Figure 19 shows the ray paths calculated with the two phase speed grids. The paths are nearly identical on this global-scale plot. (Compare the differences seen on this plot with the differences between the phase speed and channel sound speeds shown in Figure 16). For a closer look, the red-box region near Ascension Island is blown-up in Figure 20. The raypaths (at nearly antipodal ranges) are shown to be within 20 km. Given the known sensitivities of antipodal scenarios and the desired 1000 km^2 localization accuracy, the WKB approach results in a good approximation to the refracted raypaths.

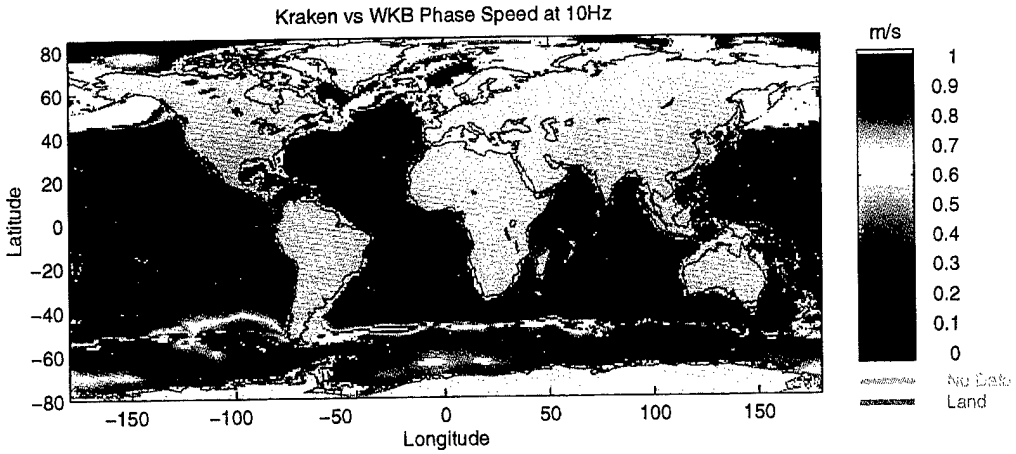

Figure 17: Kraken vs WKB phase speed for mode 1 at 10 Hz

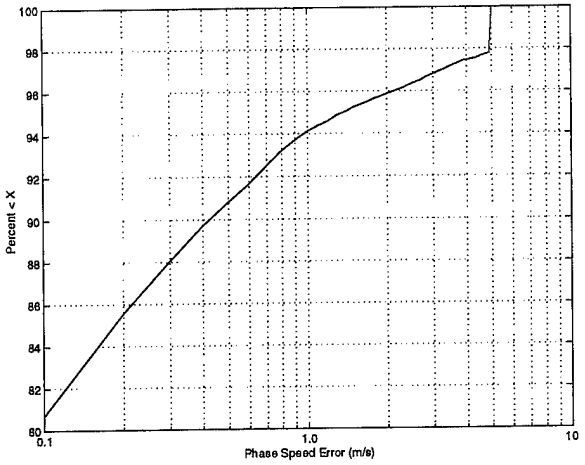

Figure 18: Cumulative distribution of phase speed errors shown in Figure 17

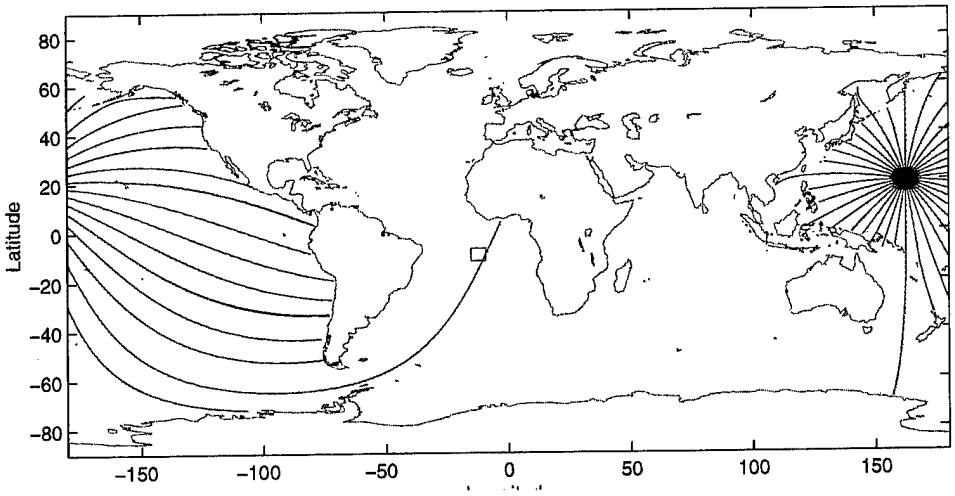

Figure 19: Ray paths calculated using WKB (blue) and Kraken (red) phase speed grids

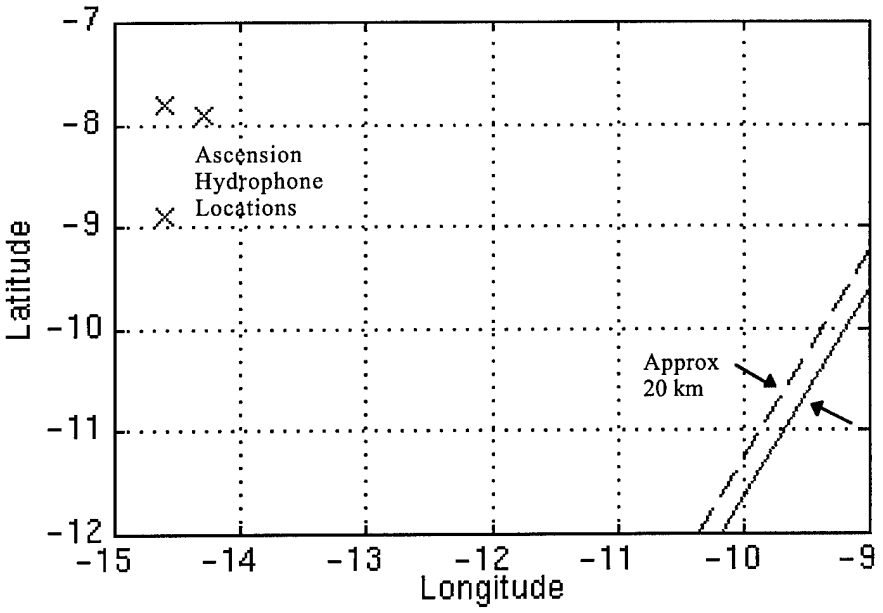

Figure 20 WKB (dashed) and Kraken (solid) ray paths near Ascension Island

3.1.8 Bending versus Shooting

The last issue relating to travel time prediction is the refinement of methods for determining ray paths between two fixed points. The usual approach is to iteratively perturb the initial launch angle from the starting point until the refracted path passes through the known receiver position. This approach can be computationally intensive in that a large number of rays may need to be traced until an acceptable solution is found. In some cases, particularly when the source and receiver are nearly antipodal, these approaches may also fail to converge without sufficient manual intervention.

As an alternative, HydroCAM includes a perturbational approach where the two desired endpoints are fixed and an initial raypath is perturbed until the travel time along the path is minimized. Figure 21 graphically illustrates the difference between the two approaches. The numbers indicate the iteration on each approach. The shooting/searching method in Figure 21(a) stops when the ray path passes close enough to the desired endpoint. The bender approach stops when the difference between successive iterations of the locations along the entire path are smaller than a user specified tolerance. The approach is discussed in a paper by Collins and Kuperman [11] where the method was used to overcome ray chaos. The use of relaxation techniques in two-point boundary value problems is discussed in detail by Press *et. al.* [12]. A complete derivation of the equations used in this approach is contained in Appendix C of the *HydroCAM Users Guide* [1].

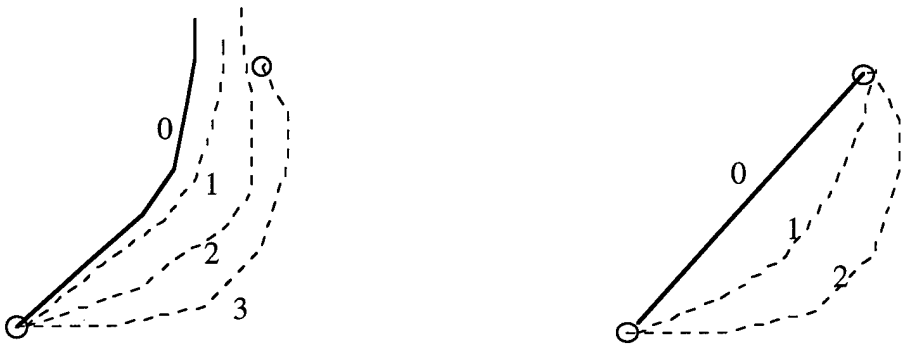

Figure 21: (a) Shooting/Searching Approach, (b) Bender Approach.

The purpose of this section is to illustrate the feasibility of applying the bending technique to global-scale monitoring predictions. The example situation shown in Figure 22 is used to evaluate the performance of the perturbation technique. The red path, which was calculated by launching a horizontally refracted ray from near Heard Island toward Ascension Island, is taken to be the ground truth. A geodesic (bottom curve) connecting the two endpoints of the refracted ray is used for the notional trajectory that initializes the bender algorithm. Note that the refracted ray travels to the north of the geodesic. This is consistent with the fact that the eigenray bends to the south as it enters the warmer northerly waters. To solve for the refracted ray using the bending approach, the geodesic is sampled at a resolution of approximately 57 km and a block diagonal system of equations solved for the perturbed path. The first perturbation to the geodesic overlays the refracted eigenray in Figure 22. Further refinements can be obtained by using the perturbed solutions as the notional trajectory for a subsequent application of the approach.

Figure 23 shows the difference between the latitude, longitude and ray angle of the eigenray and the geodesic (solid lines) and the second perturbation to the geodesic (broken lines). The geodesic strays in latitude and longitude by as much as 0.3 degrees over the trajectory, corresponding roughly to a path deviation of more than 35 km. The first perturbation to the geodesic cuts this error by a factor of ten. The second perturbation, obtained by taking the first corrected path as the notional trajectory, reduces the errors to the levels shown in the figure.

In summary, the bending approach shows promise for predicting global paths. The advantages of the approach include computational efficiency and robustness. The algorithm will be refined and used in the coming years to produce travel time grids in locations where the normal bisection raytrace has trouble converging. The conditions under which the perturbation will converge precisely to the exact answer are an ongoing subject of investigation.

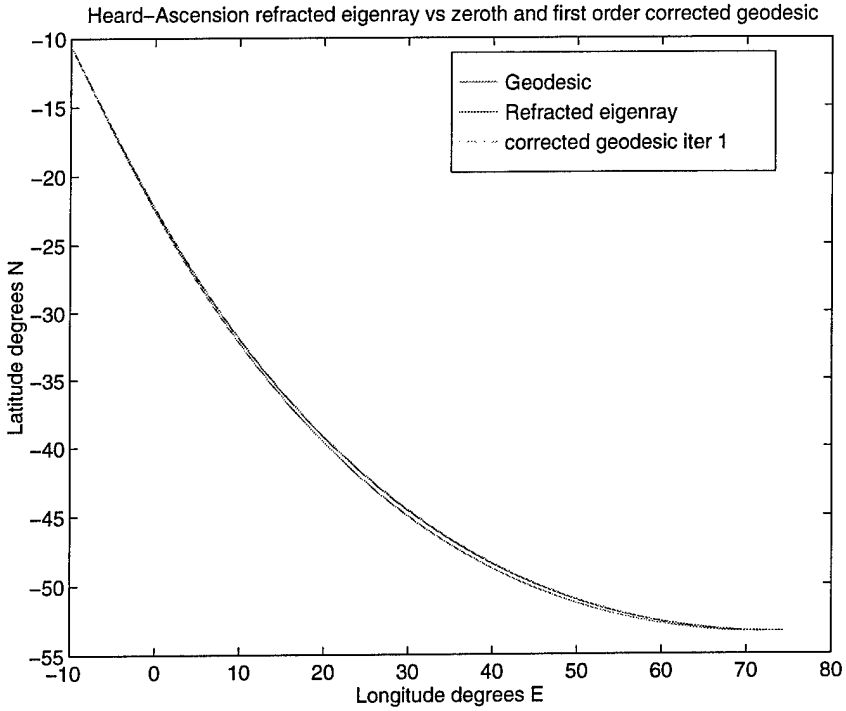

Figure 22 Geodesic (bottom), horizontally refracted (top) and the first perturbation (top) connecting the same source and receiver position near Heard and Ascension islands.

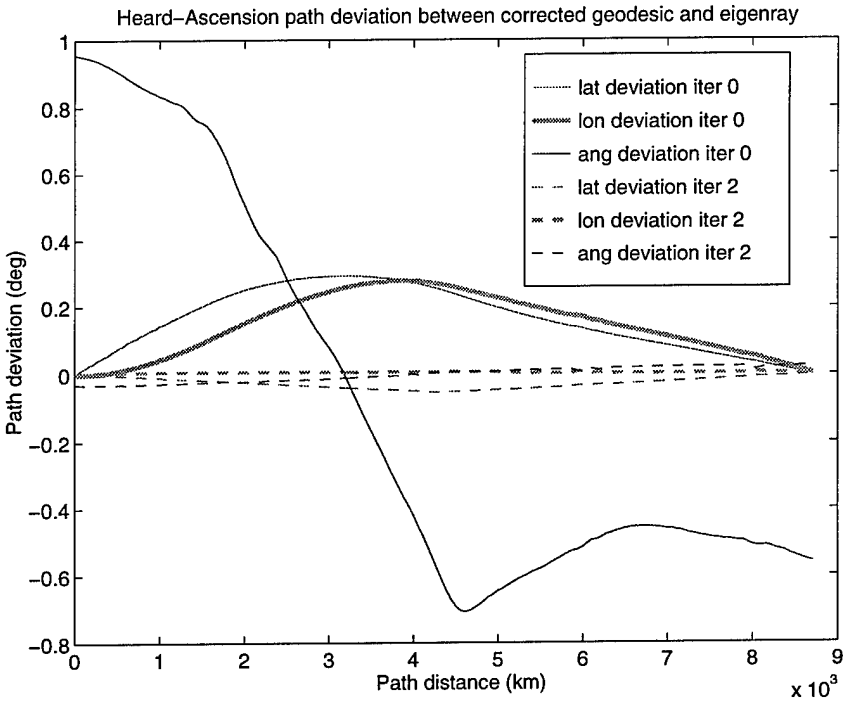

Figure 23: Difference between the uncorrected (solid) and the second perturbation (broken) to the geodesic and the ground truth refracted geodesic

3.2 Travel Time Variance

The travel time variance is an important factor in determining the performance of localization algorithms. Unfortunately, travel time variance is not a parameter normally predicted by "standard" acoustic propagation codes. Three methods were developed for HydroCAM; the path integral model, the percentage model, and the square root model.

The path integral model is a trapezoidal integration of

$$\sigma_t^2(r) = \int_0^r dl_1 \int_0^r dl_2 \sigma_s^2(l_1)\rho(l_1 - l_2)$$

where σ_s is the slowness variance calculated using either the channel model or the modal model as described in [1]. In either case, the travel time variance depends on the correlation structure of the slowness, which is currently modeled using an isotropic Gaussian correlation function, given by

$$\rho(\Delta l) = e^{-\left(\frac{\Delta l}{L}\right)^2},$$

where L is the correlation scale length in km. Researchers at the Alfred-Wegener-Institute for Polar and Marine Research have analyzed their Southern Ocean Atlas, which contains temperature and salinity measurements south of 30°S, and determined that an appropriate correlation function describing those measurements is a two-dimensional Gaussian function with latitude scale length of 350 km and longitude scale length of 450 km [13]. Since a variety of ocean conditions will produce different anisotropy (such as areas near the Gulf Stream or the Antarctic Convergence), an isotropic model with a default scale length of 300 km is used. Uncorrelated conditions are selected by setting L = 0, and totally correlated conditions are selected by setting L to a large value (much greater than the length of the longest path).

Simplified models can be obtained by appropriate choice of the correlation function. If the slowness fluctuations are assumed to be completely correlated, then the previous expression becomes

$$\sigma_t^2(r) = r \int_0^r \sigma_s^2(l) dl$$

This equation shows the travel time standard deviation is a linear function of range. Interestingly enough, early efforts in quantifying the location performance of hydroacoustic networks assumed that the travel time standard deviation was a percentage of the range [7]. This option is included in HydroCAM to allow consistency checking with those previous results.

The percentage model used in these studies was

$$\sigma_t(r) = Cr$$

where r is in units of kilometers and typical values for the constant C are from 0.01 to 0.05. If the slowness fluctuations are uncorrelated, then the expression for travel time variance becomes

$$\sigma_t^2(r) = \int_0^r \sigma_s^2(l)dl$$

and the variance is seen to be a linear function of range. In addition, when the correlation structure is represented with a triangle window, the above expression can be reduced to a constant times the square root of range. This "square root" model is used in the IVSEM model under development at Sandia National Laboratories [7], and is included in HydroCAM to facilitate comparisons with IVSEM. If the range r is in units of km, then this model is

$$\sigma_t(r) = C\sqrt{r}$$

where a typical value of C is 0.03.

Figure 24 shows an example calculation using the channel slowness variance model and equation (3). Geodesic paths were used from Ascension Island to a set of source locations on a 1 degree geographic grid. The directional variations shown in the figure are due to the geographic variations in the sound speed statistics which were included in the calculation. Favorable comparisons of this model with a limited set of measured data are provided in Section 4.0 of this report.

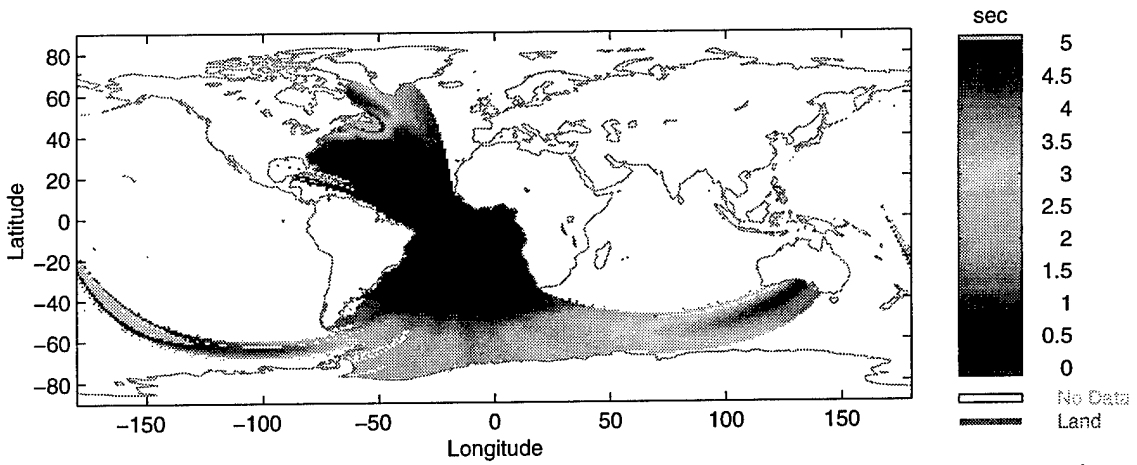

Figure 24: Example travel time standard deviation calculation for paths from Ascension Island. (The directional variations are due to the inclusion of sound speed statistics databases in the calculation.)

3.3 Source Effects and the Long-Range Starter Field

HydroCAM has the ability to introduce source "starter" fields into the Range dependent Acoustic Model (RAM) developed by NRL. The purpose is to predict the acoustic field at long ranges for distributed (non-point) sources or large amplitude sources which require non-linear propagation effects to be included. The capability to introduce a starter field, which required modifications to the RAM software, has been benchmarked by introducing a point source field at a finite range from the source. The resulting transmission loss prediction, shown in Figure 25, compares quite well with the same case generated using the PE self-starter included in the baseline RAM model. (See Figure 26)

However, significant issues remain. Of primary importance are the effects of mismatch between the propagation environment used to predict the starter field and the environment drawn from the oceanographic databases which is used for long-range propagation predictions. Since RAM is a high-angle code, much of the continuous spectrum is captured local to the range where the starter field is applied. Any starter field whose wave characteristics do not satisfy the local boundary conditions or the Helmholtz equation at the insertion point will introduce significant diffraction, producing artifacts in the predicted long-range field.

The starter field typically is generated by a two step process which links the early time, short range nuclear explosion pressures (estimated by the fully non-linear hydrodynamics code CALE) into the weak shock non-linear time domain parabolic equation code NPE, which propagates the source function to the linear regime. Since the long-range linear propagation models are narrowband, the starter-field time series must be transformed to the frequency domain. Care must be taken that the sidelobes of any low-frequency energy do not cause spurious energy at particular depths. Also, the fact that NPE is a narrow angle approximation results in distortion of the source wavefront, which introduces a violation of the Helmholtz equation. This can cause diffraction of the starter field at the point of injection. Finally, NPE requires an attenuating layer at the bottom of the computational domain. It is important that the RAM field at the point of injection also have this attenuation layer so the boundary conditions are matched.

3.3.1 Starter Field Interpolation

Another significant issue when source fields are injected into linear propagation models is the interpolation in depth that may be required. As a baseline, the source time series from CALE/NPE were provided at a depth sampling interval of 250 meters between depths of 0 and 5000 meters. Since the starter field is required at greater depth resolution by most linear propagation codes (on the order of several points per wavelength), the starter field must either be provided at a finer sampling interval or the coarse field must be interpolated.

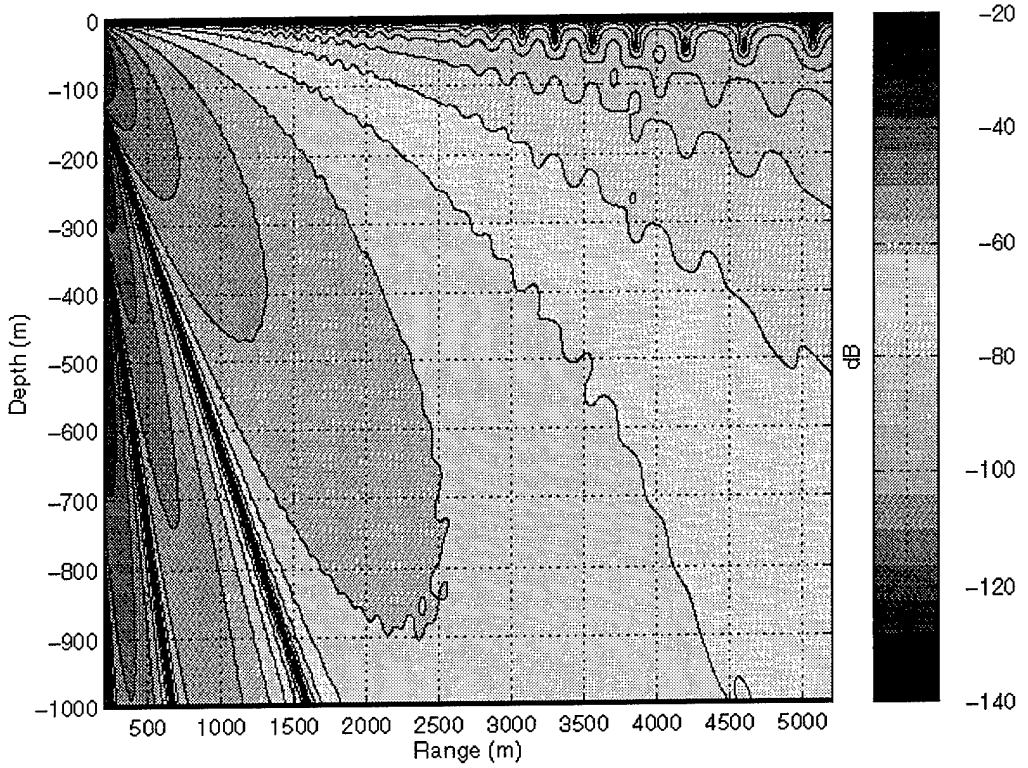

Figure 25: RAM TL prediction using BBN generated point source as starting field

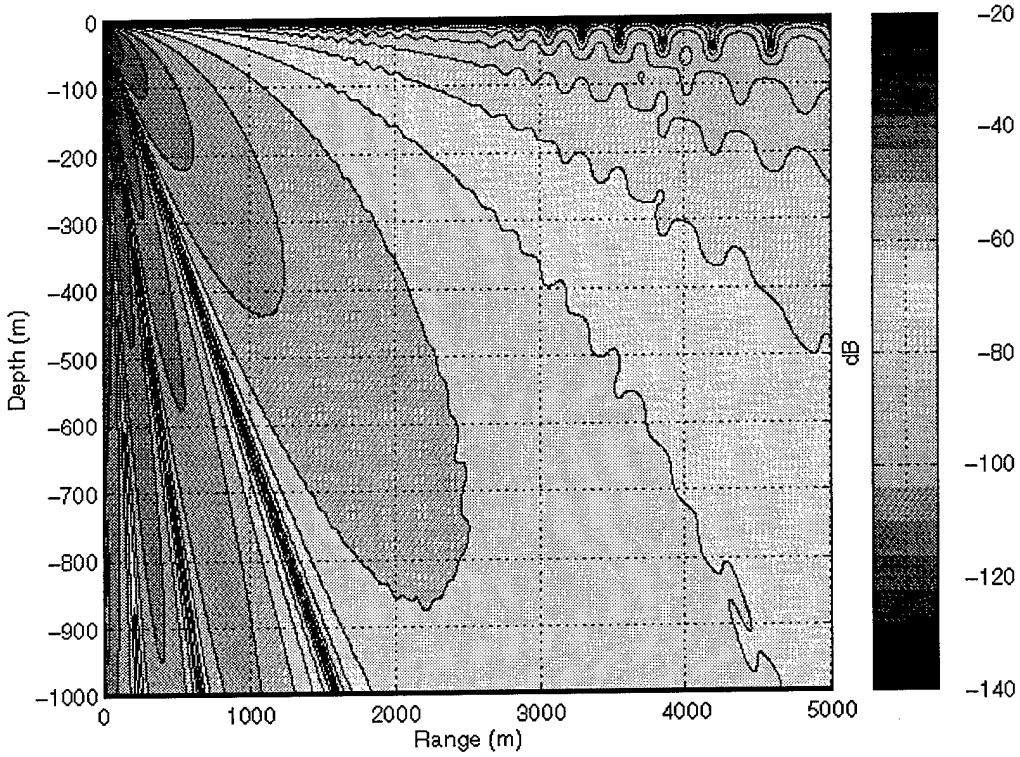

Figure 26: RAM TL prediction using Collins self-starter at 50m depth at 50 Hz

In Figure 27, the source field is shown for a 1kT nuclear explosion detonated at a depth of 50 m and a range of 10 km. The distinctive curvature of the arrival structure giving later arrival time for greater depth is due to the greater slant range of the receivers from the source location. As these calculations were performed for a typical mid-latitude sound speed profile taken from Urick [14], (see Figure 28), the wavefront deviates from the circular arrivals associated with an average sound speed of 1515 m/s superimposed on the figure. The first arrival is associated with the direct blast and the second arrival is a parasitic return from the bottom absorbing layer distributed between depths of 5000 and 6000 meters. Notice that the bottom reflection in the NPE calculation is somewhat later than the superimposed line for a sharp bottom contrast and a isovelocity sound speed profile.

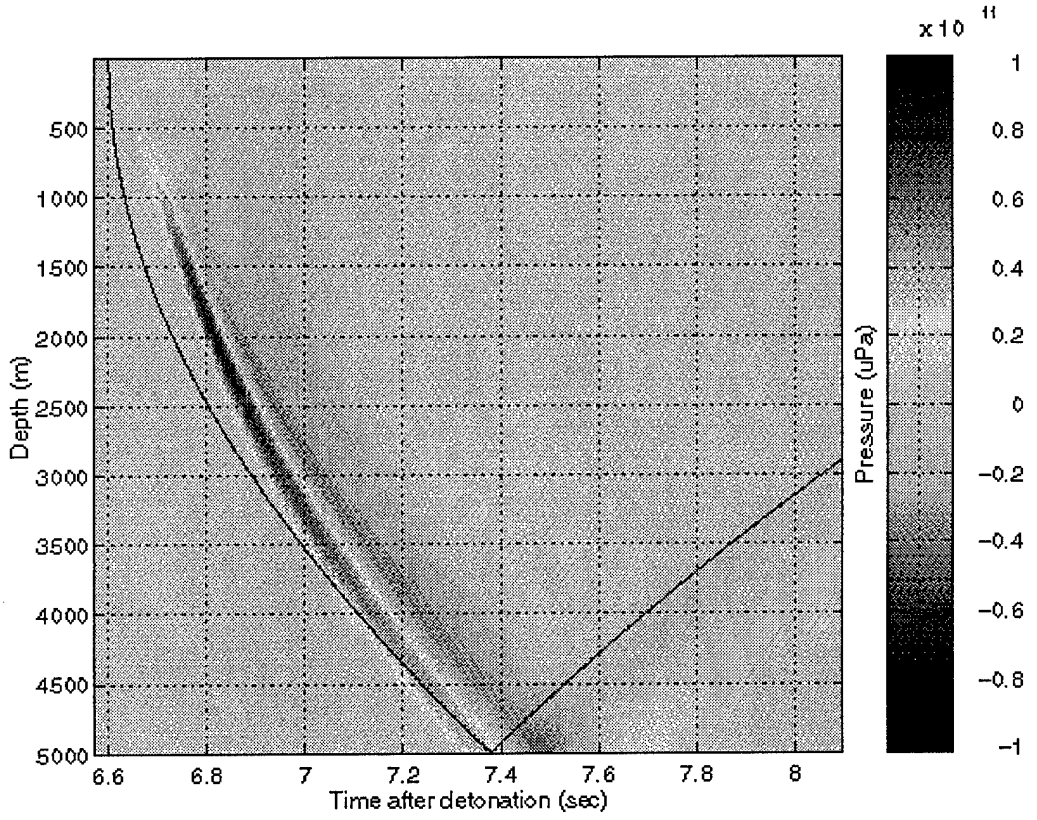

Figure 27: Pressure Time Series from CALE/NPE sampled every 10m in depth

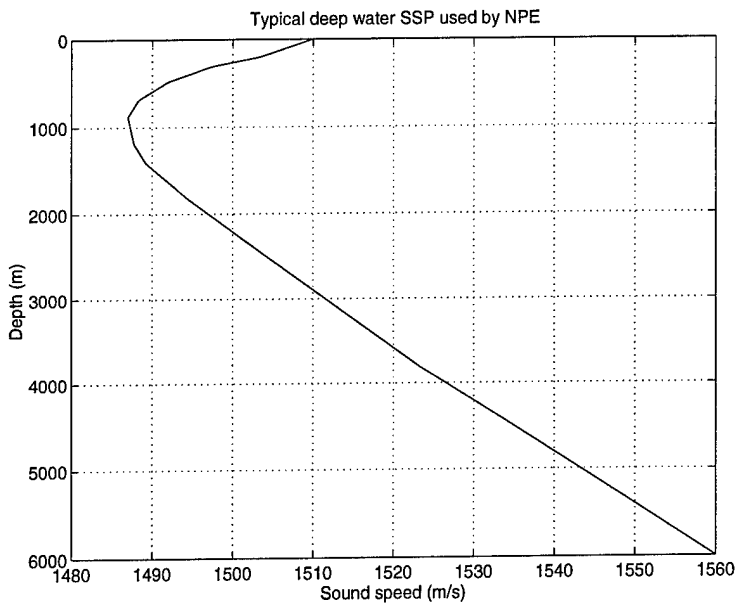

Figure 28: Sound Speed Profile Used in NPE Calculations

The desire is to interpolate a time series which is coarsely sampled in depth, such as the one illustrated in Figure 29 to obtain one which is sampled in depth with sufficient resolution for use as input to a typical wide angle PE or other type of propagation code. The most simplistic approach is to bilinearly interpolate the time series directly, but as Figure 30 shows, this approach is not adequate due to the oscillations observed in the direct arrival. What is required is interpolation which is "wave based", by which we mean a procedure that uses interpolation functions which satisfy the wave equation in the refractive water column, subject to the boundary conditions. Since the refractive waveguide is dispersive, it is best to obtain such interpolation functions in the frequency domain. The approach we adopt is modal interpolation.

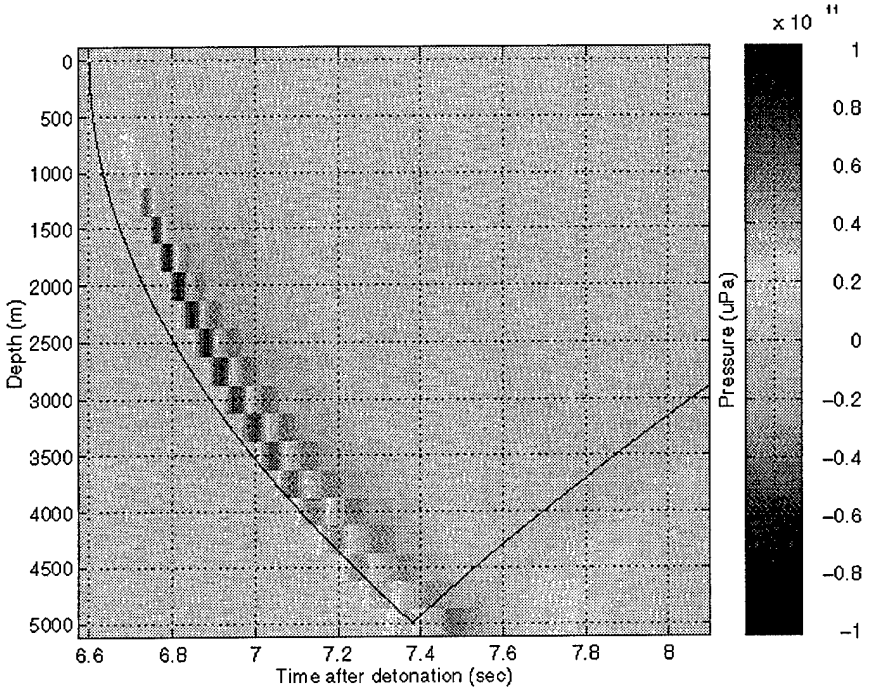

Figure 29: Coarsely sampled (250 m) pressure time series corresponding to Figure 27

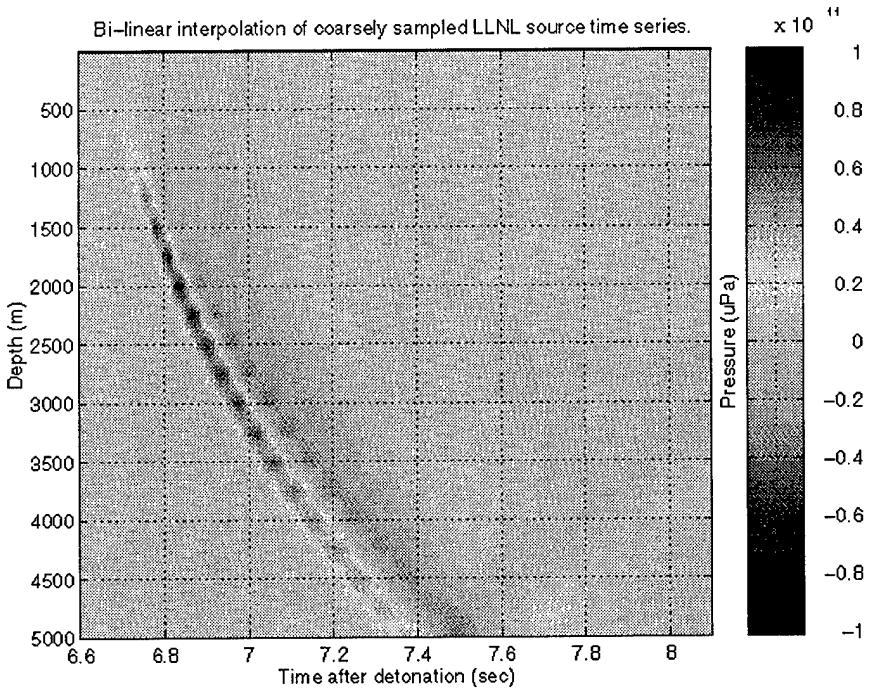

Figure 30: Bilinearly interpolated pressure time series to 10m spacing

The process of modal interpolation, which is illustrated in Figure 31, uses the normal modes $\psi_n(z)$ at the injection point as a set of basis functions to interpolate the pressure field to a new set of depths. The first step is to project the frequency-depth distribution *P(z,f)* of the starter field into the frequency-mode domain to obtain the coefficients a_n

$$a_n = \int_0^{-\infty} \frac{\psi_n(z)}{\rho(z)} P(z,f)dz$$

The mode functions are then interpolated to the new depths, z', and used reconstruct the frequency-depth distribution at these depths

$$\hat{P}(z',f) = \sum_n \frac{a_n \psi_n(z')}{\rho(z')}.$$

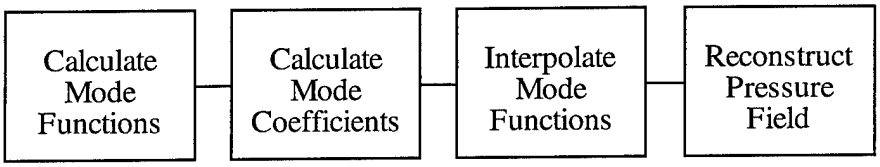

Figure 31: Modal interpolation to obtain the starter field versus depth

To pursue modal interpolation of the time series in depth, we must first recognize a couple of limitations of the technique as applied to narrow angle NPE results. First, the narrow angle PE will not correctly model the higher angle details of the propagation represented by higher order modes. Thus, it is possible that at lower frequencies there will be significant structure to the depth coefficients in a particular frequency bin which cannot be captured by the first few modes. Although propagating normal modes in a refractive half space are orthogonal, they are not complete. In order to get a complete set the entire continuous spectrum of inhomogeneous modes are needed, which in practice is impossible to obtain.

If a complete set of normal modes cannot be obtained, then the equivalence between the modal description of the field and that obtained by the PE is required to be very good. This would be true for the so called high angle PE's at a substantial range from the source, but is not true for the narrow angle PE. The rational approximation to the horizontal wavenumber used in the NPE code only does a good job for grazing angles less than approximately 15°, as is shown by the dispersive travel time of the rational square root approximation illustrated in Figure 32.

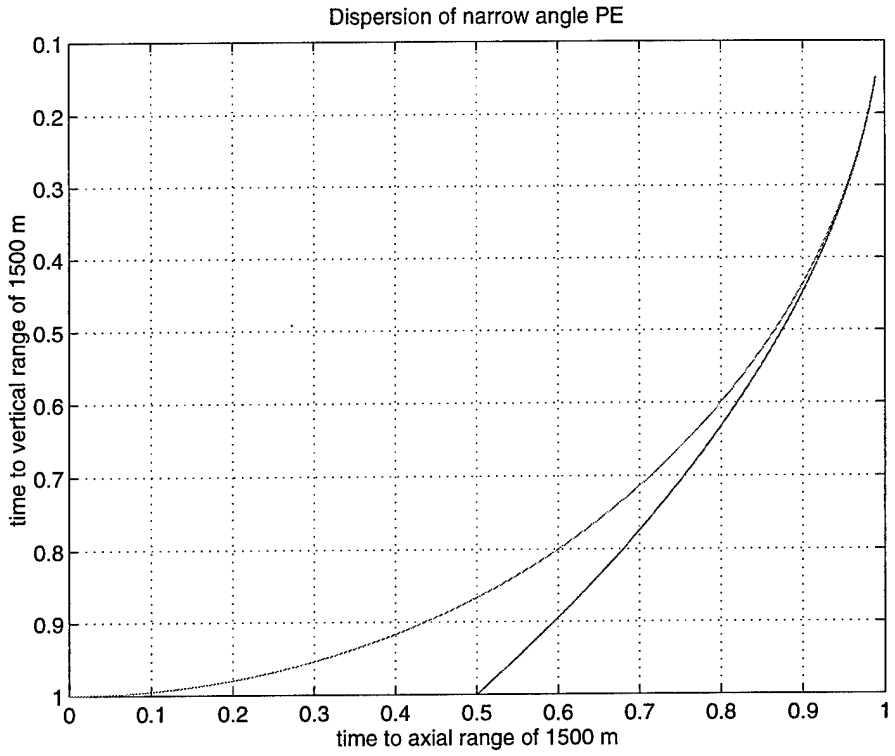

Figure 32: Time required for a pulse to travel 1500m without approximation (left) and under the rational approximation used to estimate the horizontal wavenumber from the vertical wavenumber in NPE (right). (A greater travel time means that the group speed is slower for vertically propagating energy)

Given that the linear source arrival structure is significantly different at greater depths than the CALE-NPE result, and the fact that the modes have been obtained without modeling the absorbing layer between 5000 and 6000 meters of depth, it is not surprising that a modal interpolation of the CALE-NPE time series is not successful. A first order comparison is between the energy spectra of the original and interpolated waveforms. In Figure 33 the frequency-depth decomposition of the 10m sampled CALE-NPE time series is illustrated for a temporal duration of 1 second in the upper panel. In the lower panel the best fit over the 5 to 5000 meter aperture using homogeneous modes every 10 meters is illustrated. The fit is fairly good over the middle depths but diverges below 3000 meters and above 500 meters. However, these figures compare the energy distributions. Since the goal is to interpolate a complex starter field, it is important for any comparison to include the phase as well. Figure 34 shows a plot of the complex pressure at 10 Hz corresponding to the two plots in Figure 33. As in the spectral comparison, the fit is quite good between 500 and 3000 meters.

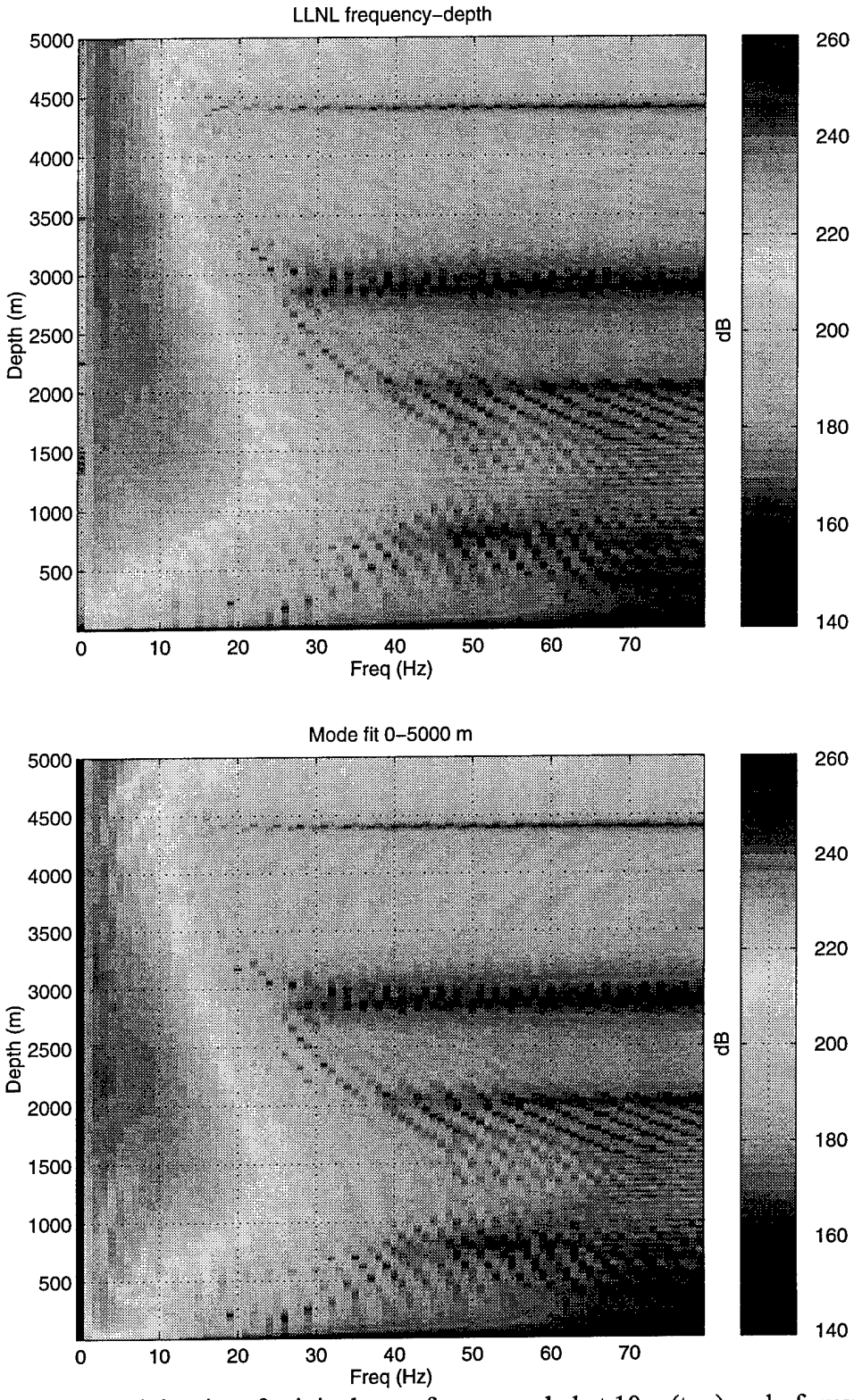

Figure 33: Spectral density of original waveform sampled at 10m (top) and of waveform reconstructed using modal interpolation to 5000m (bottom)

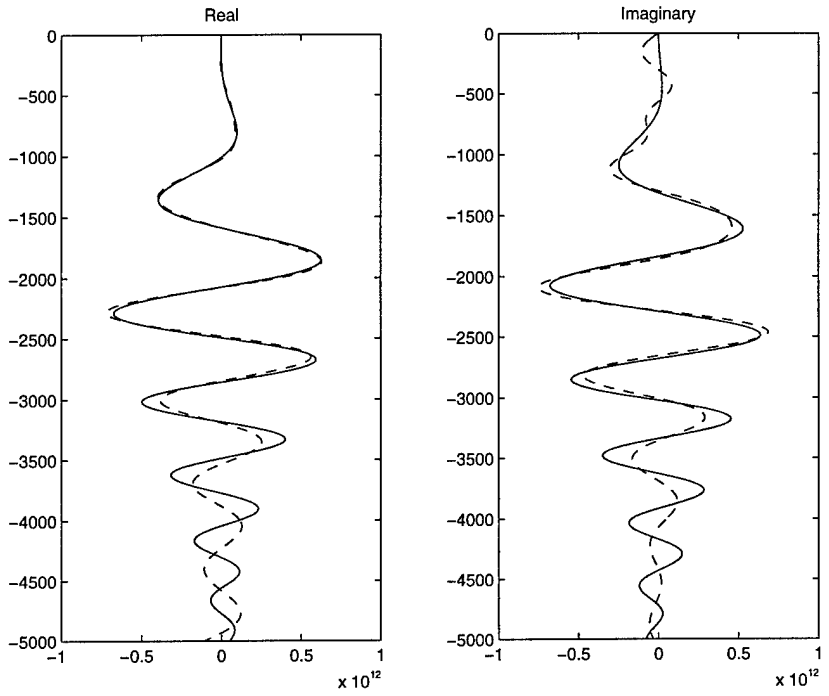

Figure 34: Complex pressure at 10 Hz from CALE/NPE sampled every 10 m (solid) and using modal interpolation on CALE/NPE decimated to every 250 m (dashed)

A further test, which includes the phase over the entire band, is to compare the predicted time series. The original 10m sample time series is illustrated in the top of Figure 35. The modal interpolation over the 5 to 5000 meter aperture using homogeneous modes is illustrated in middle panel. In this case interpolation fails at depths above 1000m and below 3000m. This is probably due to the inability of the orthogonal but incomplete mode functions to model the dispersion of the NPE and also the poor modeling of the modes of the absorbing layer. To show that a more complete set of modes results in better interpolation, a second modal fit was calculated using the first 0.8 seconds of the source function over the top 4000 meters of the water column. These two factors effectively eliminate the bottom reflection from the fit, which occurs at a later time and at shallower depths. The resulting interpolation, shown in the bottom of Figure 35, is excellent over the fitting aperture but fails at greater depths.

Modal interpolation of the CALE-NPE source function appears to work over the water column when the bottom interactions are ignored. However, the discontinuities present in the resulting waveform near the bottom will cause diffraction artifacts when the starter field is interfaced to RAM. In addition, modal interpolation that includes the bottom fails due to the inability of the modal functions to properly model the dispersion of the NPE and the reflection off the NPE absorbing layer. For these reasons, source functions must be provided from CALE/NPE to HydroCAM with adequate depth sampling.

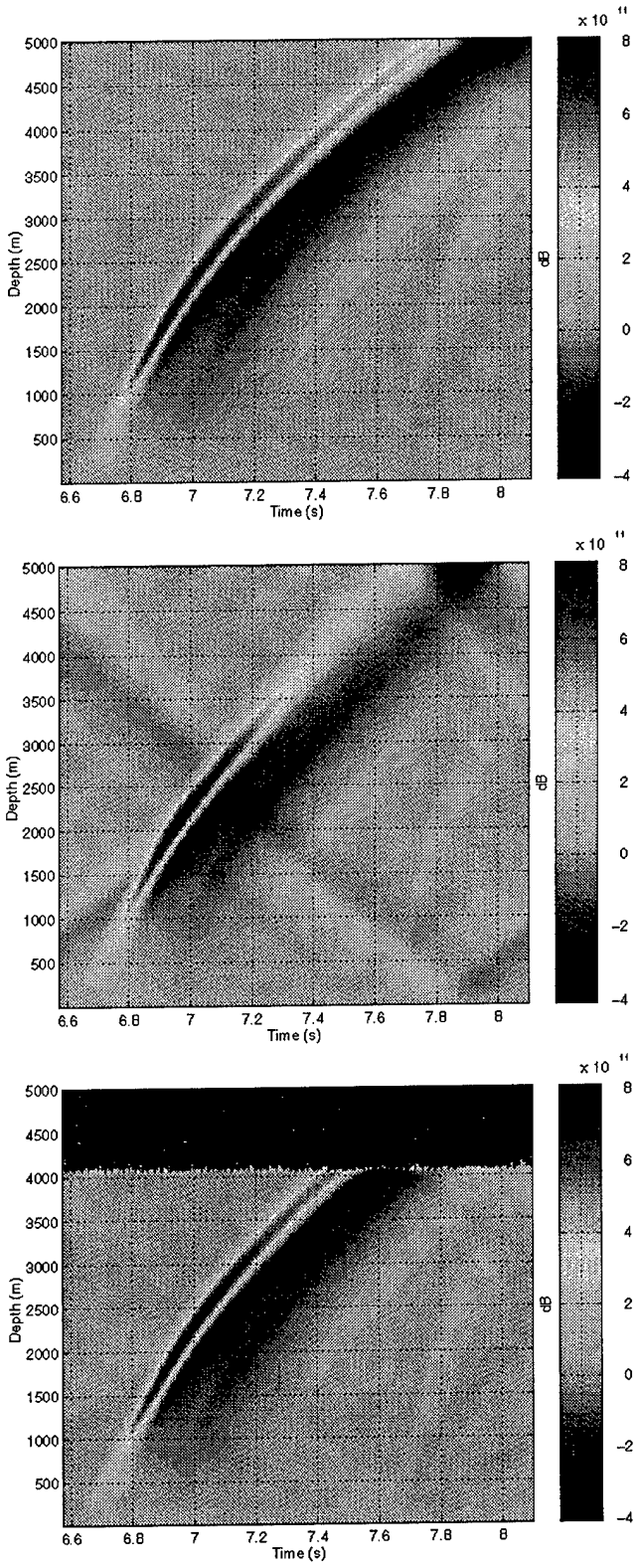

Figure 35: Pressure time series for (top) original waveform sampled at 10m, (middle) modal interpolation using entire water column and (bottom) modal interpolation with bottom interaction removed

4.0 Model Validation

One of the objectives of this effort was to validate the baseline model using measured data. Comparisons between travel time measurements taken during the Heard Island Feasibility Test [15], the French nuclear tests in 1995, and an explosion off the coast of Australia in 1960 [16] have been performed. These paths are depicted in Figure 36. Additional travel time comparisons as well as validation of the amplitude and travel time variance models will be made in the near future.

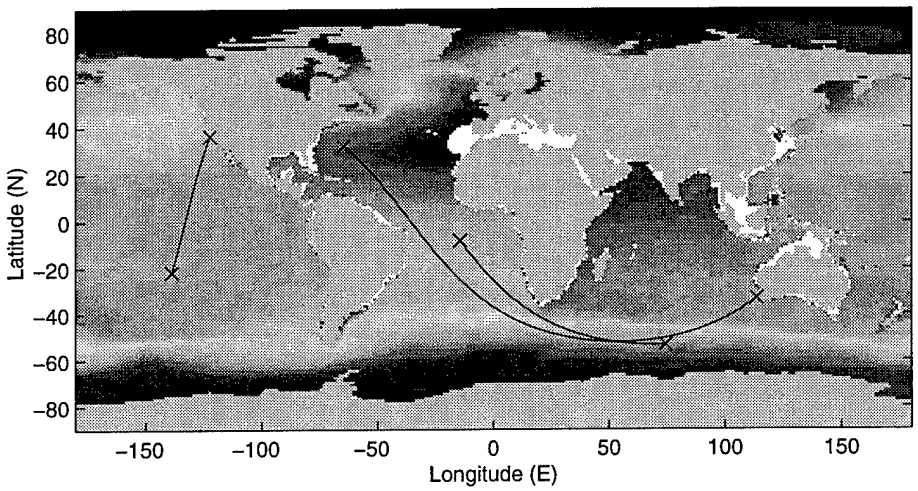

Figure 36: Three paths with measured travel time data

4.1 Travel Time

Unless otherwise specified, the procedure for predicting the travel times shown in this section is as follows:

(1) The appropriate sound speed data is extracted from the World Ocean Atlas 1994 (WOA) database, which is an update to the Levitus 1982 ocean atlas. The database contains average temperature and salinity profiles for each 1 degree geographic cell. Sound speeds are calculated using Mackenzie's equation [17] by the database extraction routines in HydroCAM. When sound speed values at the SOFAR channel depths are needed, they are calculated by searching over the each profile for the minimum value.

(2) The lat/lon coordinates of the path between the source and receiver are calculated. Both the great circle path and the geodesic path are determined using the PROJ.4 geographic projection software from the USGS [21] which is included in HydroCAM. The Clarke66 ellipsoidal earth model is used, and the radius for the spherical earth model is identical to the major axis of the Clarke66 model [21]. The step size for these

calculations is 10 nmi (approx 18.5 km). Smaller step sizes did not significantly change the predictions presented here.

(3) The sound speed at the lat/lon coordinates along the path are determined by bilinear interpolation. If there are any points without data, then the path is over land and is not used.

(4) The travel times were calculated using two methods. The first used the average sound speed, $\bar{c}$ and

$$t_{avg} = r/\bar{c}.$$

The second method integrated the slowness (the reciprocal sound speed) along the path using trapezoidal integration

$$t_{slow} = \int_S \frac{ds}{c(s)}$$

4.1.1 Heard Island to Ascension Island Path

This measurement was made as part of the Heard Island Feasibility Test (HIFT) using a 57 Hz CW transmission on 26 January 1991 [15,18]. The source and receiver coordinates are as follows:

Source location: 53° 22' S, 74° 30' E (nominal position of R/V Cory Chouest)
Receiver location: 8° 4.2' S, 14° 25.2' W (MILS hydrophone # 23)

Table 2 summarizes the results for this measurement. The predictions were made for both the surface and channel depths in January, and for the annual average of the sound speeds at the channel depths. The authors in [18] report that the first noticeable arrivals of energy during the experiment were observed at 1 hour 44 minutes and 17 seconds (6257 seconds), with multipath arrivals spread over 8-10 seconds. The predicted values for both geodesic and great circle paths using the channel sound speeds fall within these limits, from 5.1 to 9.6 seconds later than the measured first arrival. It is expected that travel times calculated using the channel depth would correspond to the latest observed arrivals since, by definition, the sound speed at the channel is a minimum. The table also shows less than 0.2 sec difference in the predicted arrival times between the averaging and integrating methods for using the channel sound speeds, and several second differences using the surface sound speeds. This is due to the relatively large variation of the surface sound speed over the path. Since the geodesic and spherical earth paths connecting the source and receiver are nearly identical, as shown in Figure 37, the approximately 3.3 second difference between them is due to the difference in the geometric path lengths.

Table 2: Difference Between Predicted and Measured Travel Times
Heard Island Source and Ascension Island Receiver

Predicted-Measured (seconds)

Sound Speed Data (WOA)		Great Circle (9235 km)		Geodesic (9230 km)	
Month	Depth (m)	t_{avg}	t_{slow}	t_{avg}	t_{slow}
January	0	-115.6	-113.6	-118.4	-116.6
January	Channel	8.4	8.6	5.1	5.2
Annual	Channel	9.4	9.6	6.2	6.4

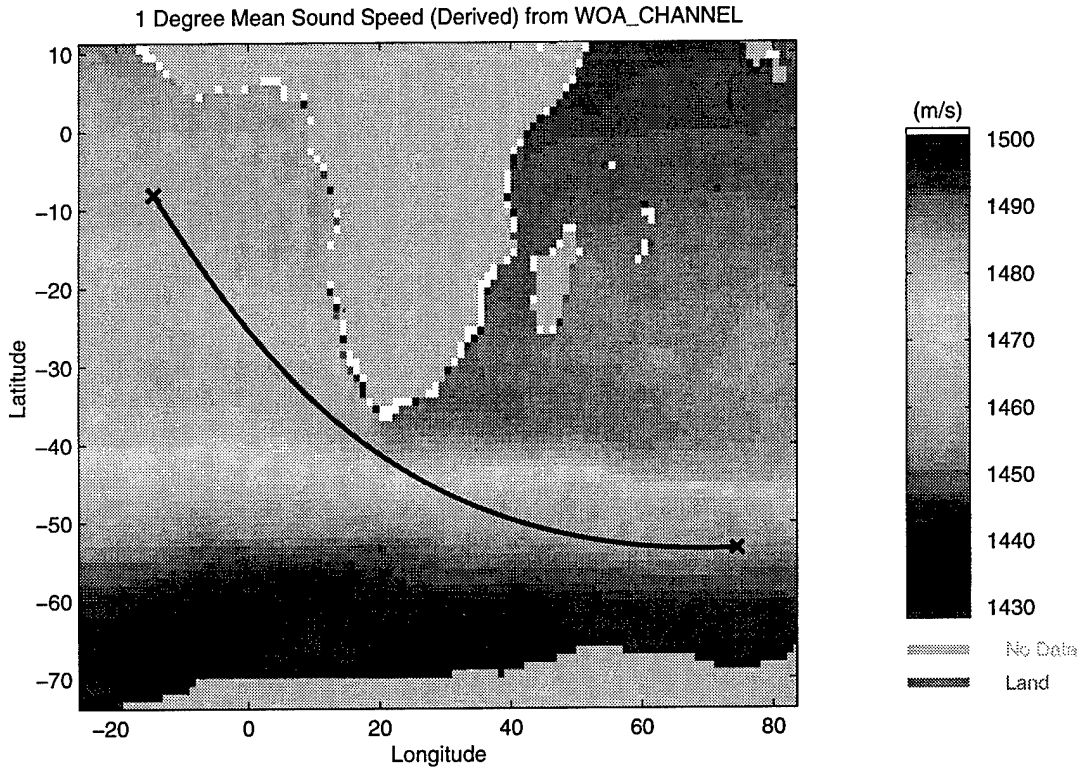

Figure 37: Heard-Ascension Path

4.1.2 Perth, Australia to Bermuda Path

These measurements were made on March 21, 1960 using 300 lb explosive charges dropped from the Australian ship HMAS Diamantina off the coast of Australia [16].

Figure 38 shows the source, receiver and both the great circle and geodesic paths between these points. Note that in this case, the geodesic path goes significantly south of the great circle path, and therefore samples colder water with slower sound speeds. The source and receiver coordinates are as follows:

Source location: 33° 13' S, 113° 43' E (nominal HMAS Diamantina position)
Receiver location: 32° 10' N, 64° 35' W (nominal Bermuda Hydrophone position)

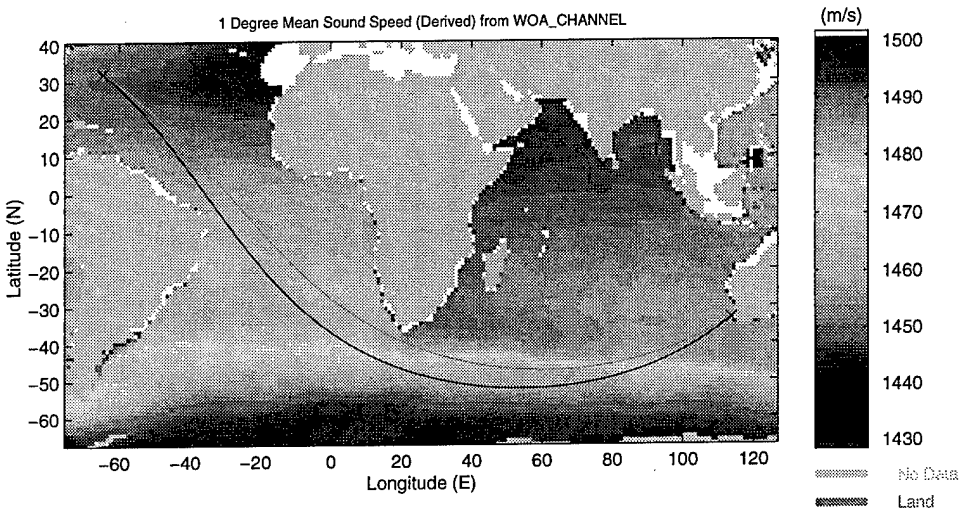

Figure 38: Geodesic (bottom) and spherical (top) paths for Perth-Bermuda measurement

Table 3 summarizes the difference between the predictions and the first measured arrival at 13 364 seconds. Compared to the Heard-Ascension path (Table 2), Table 3 shows larger differences in the predicted arrival times between the averaging and integrating methods. This is due to both the longer path length of Perth-Bermuda and the larger sound speed variability along the paths. There are also significant differences between the geodesic and great circle paths since sound speed along the paths is significantly different (See Figure 38). In addition, none of the predicted travel times correspond to the three arrivals measured during the experiment (which occurred at 13 364, 13 373, and 13 375 seconds). This is most likely due to horizontal refraction away from the geodesic path.

Table 3: Difference Between Predicted and Measured Travel Times
Perth-Bermuda Path

Predicted- Measured Time of First Arrival (seconds)

Sound Speed Data (WOA)		Great Circle (19,840 km)		Geodesic (19,821 km)	
Season	Depth (m)	t_{avg}	t_{slow}	t_{avg}	t_{slow}
March	Channel	33.6	34.0	52.3	53.0
Annual	Channel	31.9	32.3	52.7	53.5

The horizontal refraction models included in HydroCAM were also compared against this data. (Recall that this approach was used successfully in Reference 8). Global phase speed and group speed grids at 1 degree resolution were constructed using the Kraken normal mode model and the annual average sound speed profiles from the WOA database. In addition, 5 minute resolution grids were produced around Kerguelen Island, Crozet Island, the eastern coast of Brazil and the southern coast of Africa (See Figure 39). The high resolution grids used the ETOPO5 bathymetry database and bilinear interpolation of the WOA sound speed profiles. Since most of the energy from a 300 lb explosive charge is expected to be at low frequency, these grids were produced at 10 Hz, for mode 1 only.

Figure 39 shows several eigenrays connecting the Diamantina source and the Bermuda hydrophone. The parameters of these ray paths are summarized Table 4. The predicted travel time of some of these rays are closer to the measured data than the geodesic or great circle paths. Paths 1 and 2 are within the predicted standard deviation of the measured travel time. Paths 3, 4 and 5 probably correspond to the second arrival of energy observed [8]. Further refinements to the predictions will be difficult for this case, due to the expected travel time variance and the antipodal sensitivities.

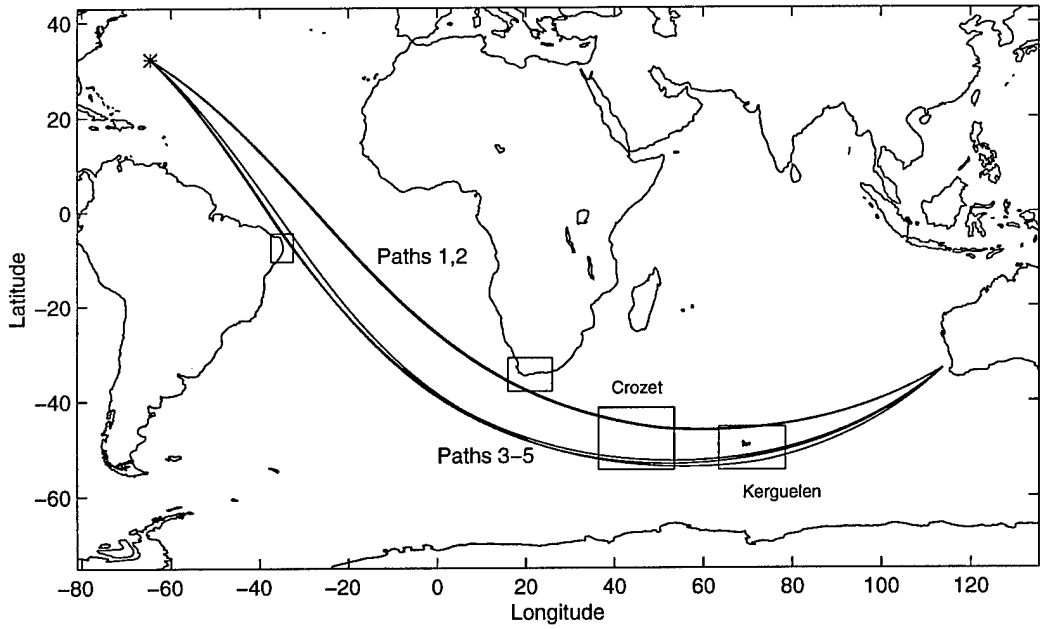

Figure 39: Mode 1 eigenrays between Perth and Bermuda. High-resolution grids are shown by boxes.

Table 4: Difference Between Predicted and Measured Travel Times
Perth-Bermuda Path

including the effects of horizontal refraction for mode 1 at 10 Hz

Path Number	Launch Angle (deg)	TL (dB)	t_{slow}-13,364 (sec)	σ_t (sec)
1	235.54	175.1	4.2	3.6
2	235.76	174.1	3.2	3.7
3	222.52	179.7	50.0	3.9
4	224.73	183.4	52.5	3.8
5	225.55	182.6	51.1	3.9

4.1.3 Mururoa Atoll to Pt Sur, California

This measurement was made at a single hydrophone off Pt Sur, California from the French underground nuclear test at Mururoa Atoll on 5 September 1995. The waveform data and receiver coordinates were obtained from the International Data Center (IDC) web page. The source coordinates are approximate; they were determined using the DMA developed Digital Chart of the World and checked with the IDC event bulletin for consistency. The source and receiver coordinates used for the predictions are:

Source location: 21° 49.8' S, 138° 48.0' W (Mururoa Atoll)
Receiver location: 32° 18.1' N, 122° 23.6' W (Pt Sur Hydrophone)

Figure 40 shows the source, receiver and both the great circle and geodesic paths between these points. As in the Heard-Ascension test, the geodesic and great circle paths are nearly identical in lat/lon. However, the geodesic path is approximately 36.1 km shorter than the great circle path due to the varying "radius" of the ellipsoidal earth. (See the *Travel Time Bias* section for additional comparisons between geodesic and great circle paths). Once again, the predictions were made for the month in which the experiment occurred (September) and for the annual average of the sound speeds at the channel depths. Analysis of the waveforms obtained from the IDC showed that the first arrival occurred about 4492 seconds after the shot time, with significant energy continuing for about 8 to 10 seconds after the first arrival. The comparisons of the predicted travel times with the first measured arrival time are listed in Table 5. The geodesic model clearly predicts the travel time as well as can be expected, given the uncertainty in the source coordinates and origin time. The accuracy in this case is likely due to the mid-latitude path, which does not traverse through significant changes in channel sound speed, channel depth, or interact with bathymetry.

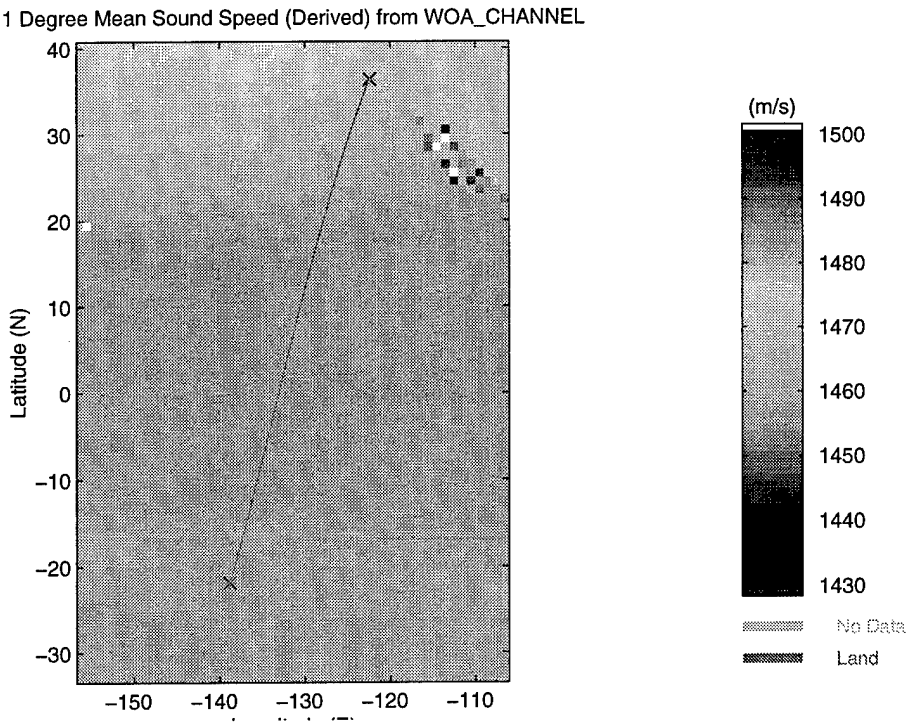

Figure 40: Mururoa to Pt Sur Path

Table 5: Difference Between Predicted and Measured Travel Times
Mururoa-Pt Sur Path

Predicted- Measured Time of First Arrival (seconds)

Sound Speed Data (WOA)		Great Circle (6697.5 km)		Geodesic (6661.4 km)	
Season	Depth (m)	t_{avg}	t_{slow}	t_{avg}	t_{slow}
September	Channel	23.4	23.4	-1.0	-1.1
Annual	Channel	23.8	23.8	-0.6	-0.6

4.2 Travel Time Variability

During a portion of the Acoustic Thermometry of the Ocean Climate (ATOC) experiment, the travel time of an M-sequence coded waveform was measured by a vertical array deployed off the coast of Hawaii. The source was located on the R/V Flip off the coast of California. Measurements of the peak energy received in each beam of the vertical array (after matched-filtering of the M-sequence waveform) were provided by WHOI for an eight-day time period [19]. (See Figure 41 below). The travel time variance

prediction for HydroCAM is approximately 0.5 seconds along this path, which corresponds well with the spread of the near-horizontal arrivals shown in Figure 41. It should be noted that the standard deviation predicted by HydroCAM does not include the effects of waveform dispersion, whereas the peaks shown in the figure include both waveform dispersion ("picking error") and the travel time variance due to sound speed fluctuations during the eight-day experiment. The travel time predicted by HydroCAM for this path is 2196.4 seconds.

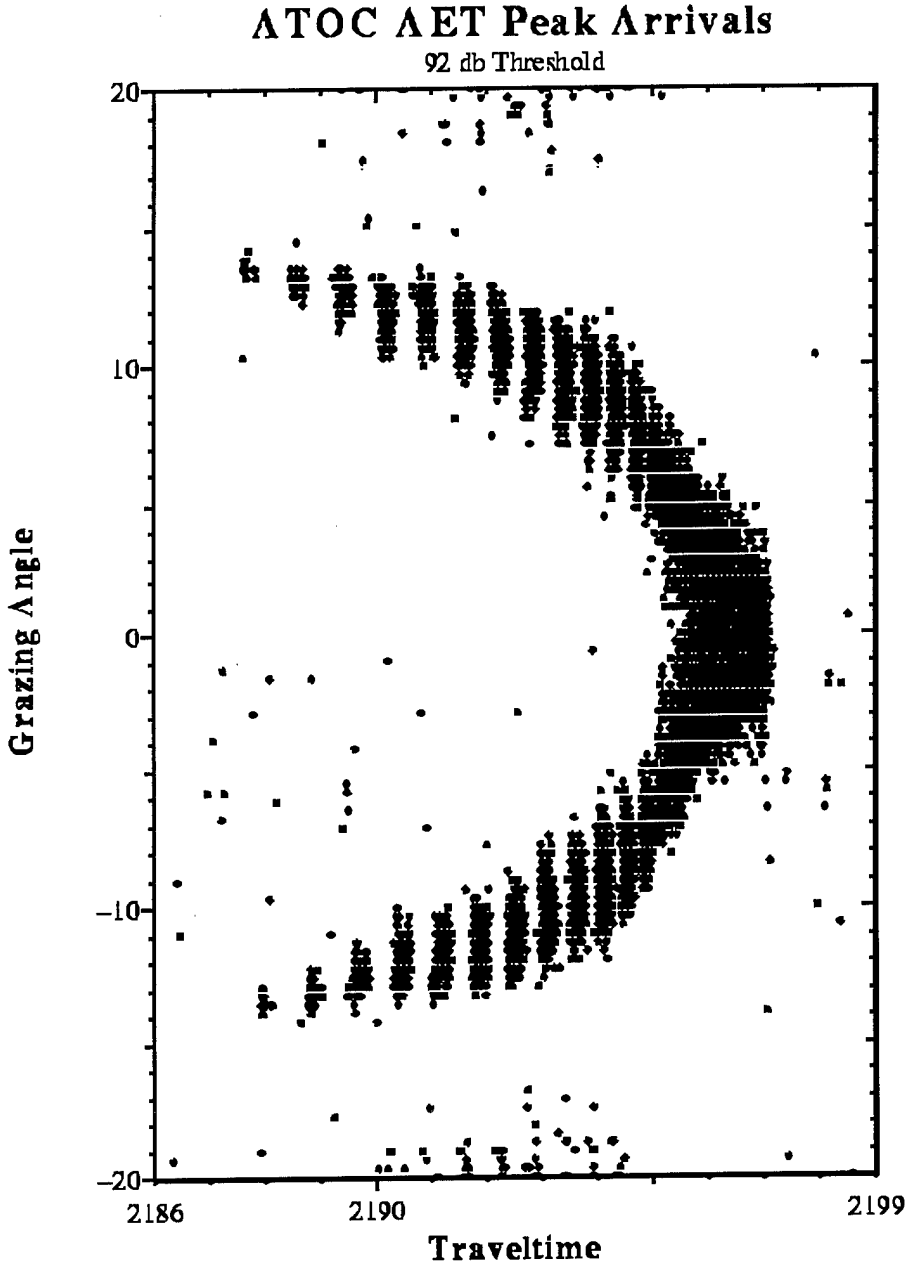

Figure 41: Peak arrivals detected on a vertical array deployed near Hawaii from a source off the coast of California during an eight-day period. (Figure courtesy of WHOI [19]).

5.0 Example Applications

Two example applications of the HydroCAM model are now presented. The first shows the detection and localization coverage of the candidate IMS. The second application is to look at the details of the coverage in a region where the first analysis indicates there may be gaps in the coverage.

5.1 Detection and Localization Coverage of the IMS

In this example, the detection and localization coverage of the candidate IMS will be predicted under annual average ocean conditions. Since the effects of horizontal refraction and seasonal variability are neglected in this example, it should be considered as illustrative only. Table 6 lists the locations used for each station. A map showing these locations is provided in Figure 42.

Table 6: IMS Hydroacoustic Station Locations [20]

Station	Latitude Deg N	Longitude Deg E	Type†
Tristan da Cunha	-37.20	-12.50	SS
Clarion Is.	18.20	-114.60	SS
Queen Charlotte Is.	52.10	-131.50	SS
Guadeloupe	16.30	-61.10	SS
Flores Island	39.30	-31.30	SS
Juan Fernandez 2	-33.90	-78.80	SH
Juan Fernandez 1	-33.30	-78.80	SH
Crozet 2	-46.70	51.70	SH
Crozet 1	-46.30	52.20	SH
BIOT/Chagos 2	-7.60	72.50	SH
BIOT/Chagos 1	-6.30	1.00	SH
Cape Leeuwin	-35.00	114.20	SH
Ascension 3	-7.90	-14.30	SH
Ascension 2	-8.90	-14.60	SH
Ascension 1	-7.80	-14.60	SH
Wake Island	19.30	162.60	SH

† SS = Island Seismic (T-Phase) Station, SH = Hydroacoustic Station

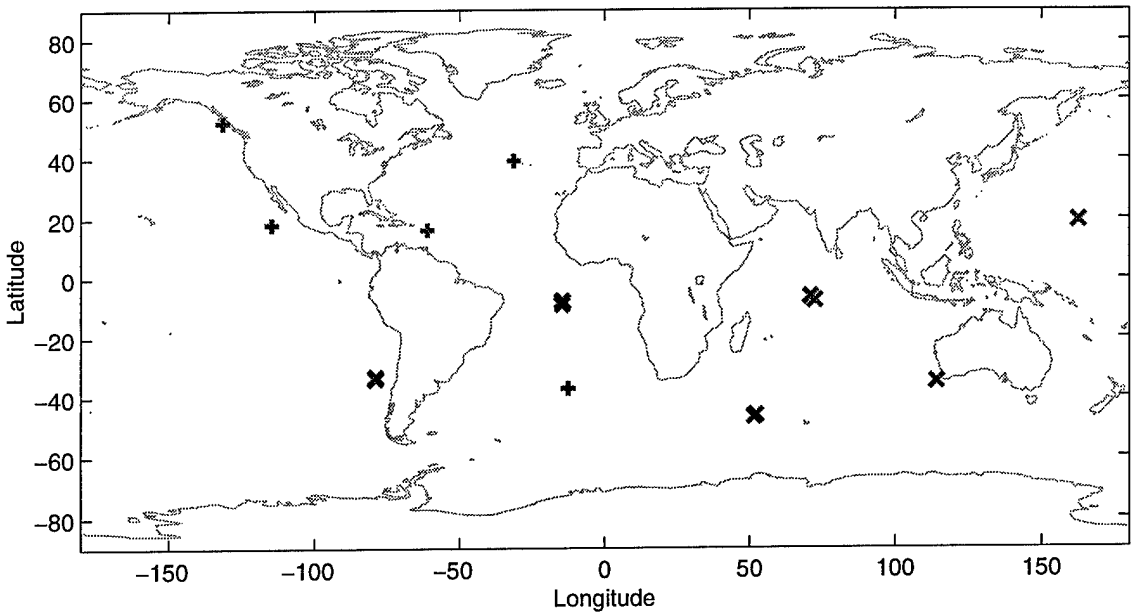

Figure 42: IMS Hydroacoustic (X) and Island Seismic (+) Stations

The first step in the prediction is to run the path model to calculate the travel time, transmission loss and travel time standard deviation from each receiver in the network to a grid of source locations. The parameters used in this run are summarized in Table 7. The resulting transmission loss (path attenuation) and travel time standard deviation for the Cape Leeuwin station are shown in Figure 43 and Figure 44, respectively.

The SNR calculation is the first function performed in the network performance model. For the example shown in Figure 45, the SNR model is an energy form of the passive SONAR equation

$$SNR(f) = ESL(f) - TL(f) - (NL(f) + 10 \log T) + AG(f) - L(f).$$

ESL is the energy spectral level of the source (*dB re* μPa^2 *sec*) at a reference distance of 1 meter in a 1 Hz band. TL is the transmission loss (path attenuation) calculated by the path model. It is expressed in dB relative to the energy level at 1 meter. The remaining terms describe the capabilities of each receiving station. The noise power spectral level, *NL* (*dB re* μPa^2 *in a 1 Hz Band*) was calculated using the Wenz model for a wind speed of 10 knots and a shipping level of 1 (low shipping density). AG is receiver spatial processing (array) gain, which is zero for the omnidirectional sensors in this example. *L* is the "system loss factor" which contains all processing gains and losses not accounted for elsewhere. *L* is zero for the hydroacoustic stations, and is set to 40 dB for the T-phase stations [7]. *T*, the receiver integration time in seconds, was set to 10 seconds. In general T should be set to a value that is at least as large as the time duration of the expected received signal.

Table 7: Parameters used for Example IMS Coverage Analysis

Path Model Parameters	
Grid	1 degree global grid
Path Type	Geodesic (ellipsoidal earth), 30 km step size
Frequency	10 Hz
Phase and Group Speed	Annual average sound channel from WOA94
Path Attenuation Model	Spreading, absorption and bottom attenuation
Bottom Attenuation	10 Hz, mode 1 attenuation calculated by Kraken
Ocean Depth	ETOPO30 database
Sound Speed Fluctuations	Sound channel model using WOA annual statistics
Sound Speed Horiz Correlation	Isotropic Gaussian , length scale of 300 km
Network Performance Model Parameters	
Source Level	280 dB (underwater 1kT explosion at 50 m depth)
Station Ambient Noise	Wenz model, Wind Speed 10 Knots, Shipping 1
SNR to contribute measurement	10 dB
T-Phase SNR loss	40 dB relative to Hydroacoustic
Travel Time Gradient Model	Analytic
Picking Error	1 sec for Hydro stations, 5 sec for T-Phase stations

HydroCAM uses a user specified SNR threshold to make a detection decision, primarily to determine which receivers detect the source and can make accurate arrival time estimates which contribute to a localization solution. The receivers exceeding the threshold are therefore called *contributing receivers*. For this case, the detection threshold was set to 10 dB, which results in the contributing receivers shown in Figure 46. If the signal plus noise statistics are known, then this threshold can be set to obtain a specified probability of false alarm and probability of detection using standard formulas from detection and estimation theory [25]. Depending on the choice of threshold, this grid can be used as a network detection coverage map, or as a tool to understand the contributions of each receiver in the network to the localization performance.

The final output product for this example is the Area of Uncertainty coverage map shown in Figure 47. This figure was produced by calculating the Cramer-Rao Lower Bound on the area of the 90% confidence localization error ellipse for a source at each point in the grid. The arrival time errors are modeled as a sum of the travel time error computed by the path model (see Figure 44) and the arrival time measurement or "picking error" due to waveform dispersion and SNR. The picking error was set to 1 second for hydroacoustic stations and 5 seconds for T-phase stations based on empirical data [7].

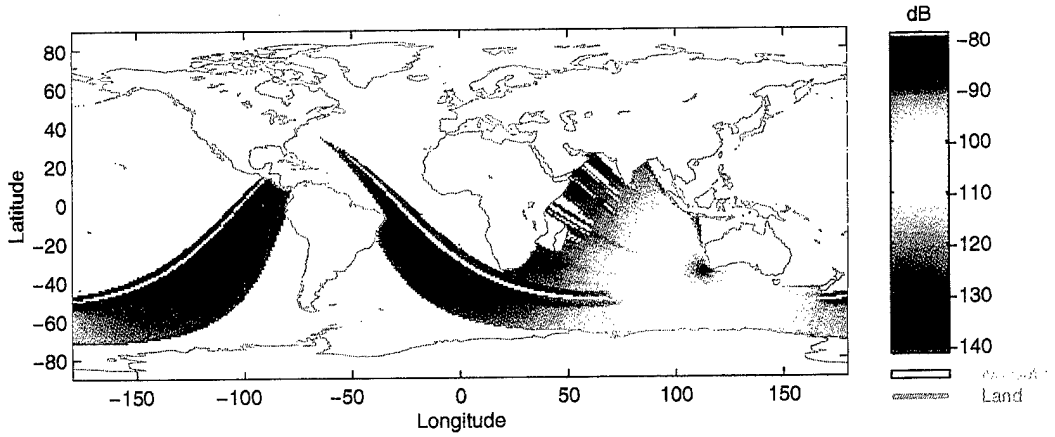

Figure 43: Path attenuation

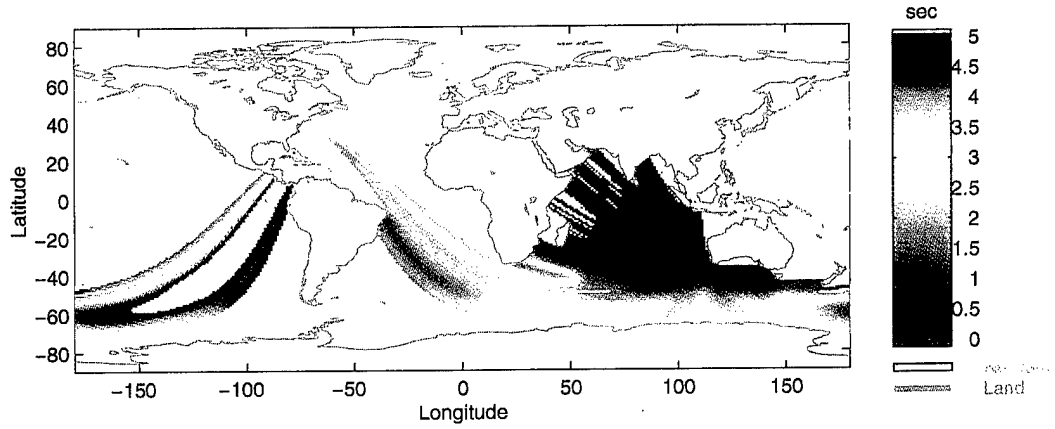

Figure 44: Travel time standard deviation

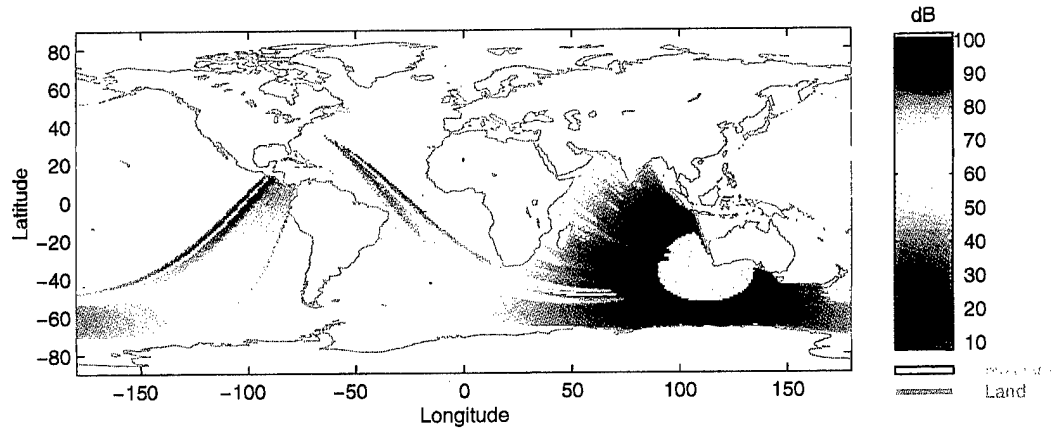

Figure 45: Signal to Noise Ratio

Figure 47 shows that large expanses of ocean can be monitored with better than 1000 km^2 localization accuracy. However, there are notable regions in the South Pacific Ocean where the blockage from islands reduces the number of contributing receivers and degrades the localization accuracy that can be obtained. These areas will be investigated in more detail in the next section.

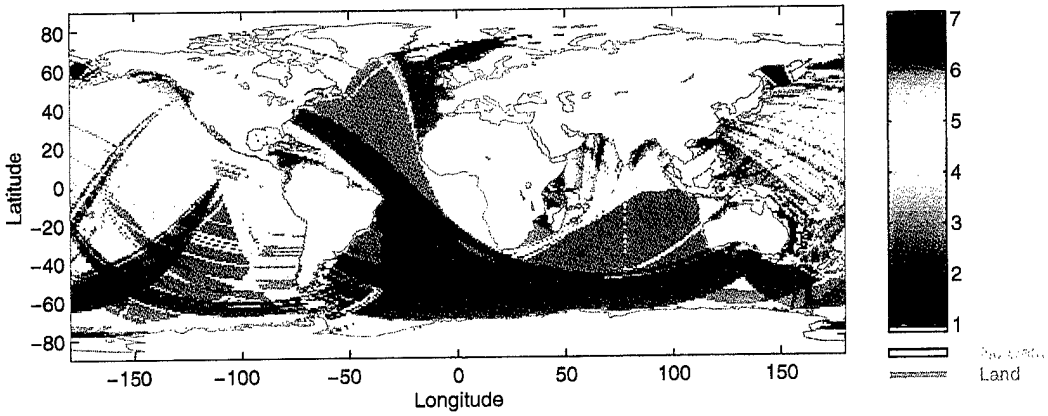

Figure 46: Number of contributing receivers

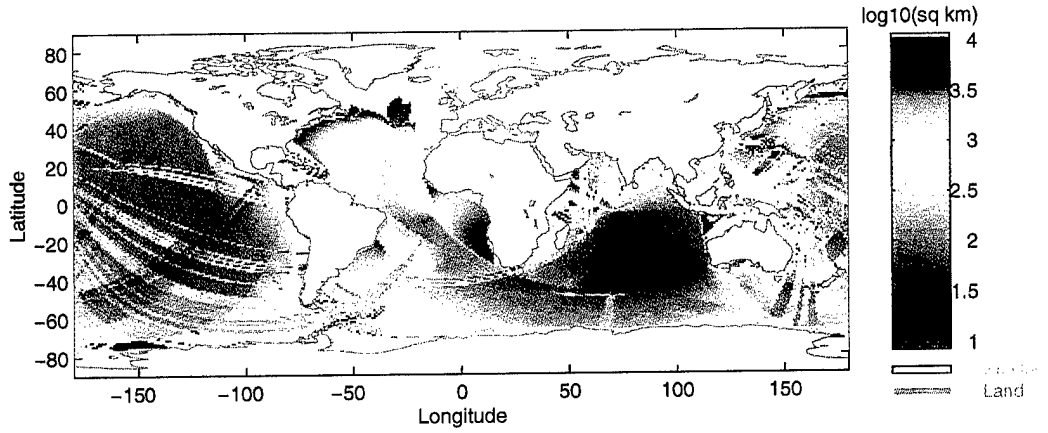

Figure 47: Area of Uncertainty

5.2 Gap Analysis in the Pacific Ocean

An inspection of the IMS network performance shown in Figure 47 reveals a number of areas where the localization performance is predicted to be much worse than the desired 1000 km^2. A blowup of the coverage in the South-East Pacific Ocean, shown in Figure 48, points to two areas of concern. The first, shown in the middle of the figure, is not likely to be a problem area since high shipping activity off the western coast of South America makes the possibility of a covert nuclear test is this area unlikely. The second area, which is a narrow arc closer to Antarctica (see the two red markers in the lower portion of the figure), may be of greater concern. A "gap analysis" of this area is desired to determine (1) the reason for the poor predicted network performance and (2) verify the location and nature of the gap. Additional analyses could then be performed to determine what measures could be taken to reduce or eliminate the gap. Example corrective measures would include small changes in hydrophone locations or the addition of a new station.

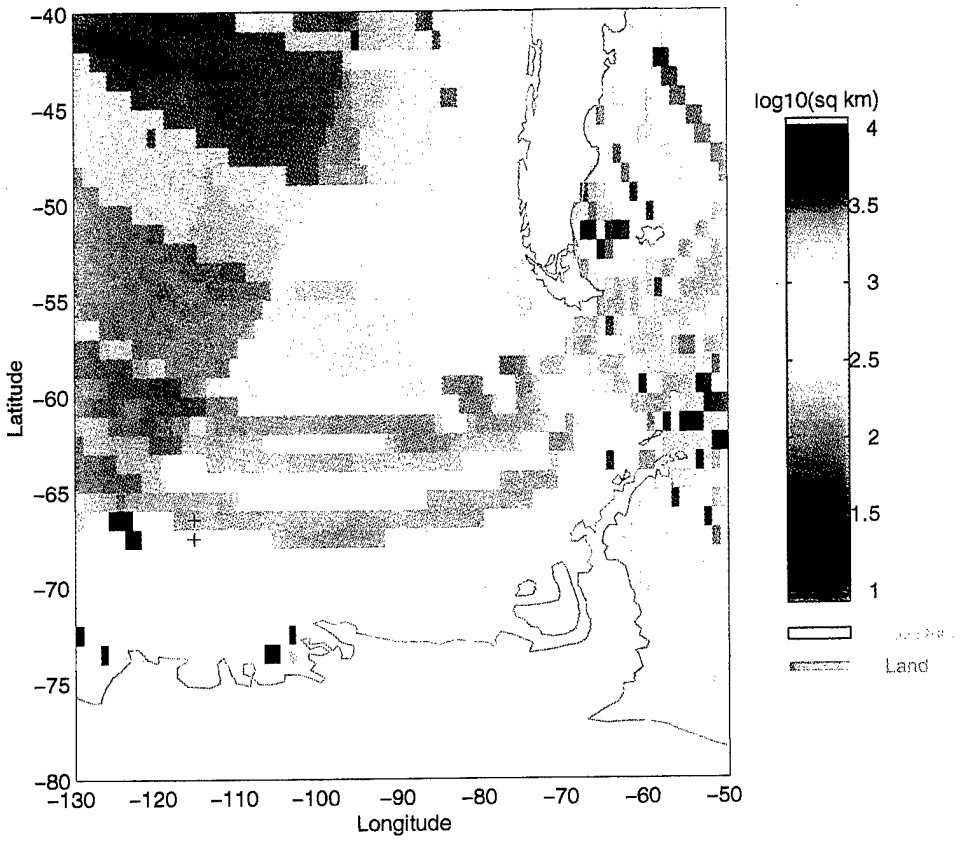

Figure 48: Predicted IMS Localization Performance in the South East Pacific

Figure 49 shows a summary of the network performance for a source located just above the gap (See the top red "+" in Figure 48). The source is detected at 8 of the IMS hydrophones, with a good distribution of angles. This situation results in a relatively low AOU. The network performance for a source in the gap, (the bottom red "+" in Figure 48) is illustrated in Figure 50. The Wake Island and Ascension Island stations are blocked from this source, resulting in a narrow set of angles to the source and a poor AOU.

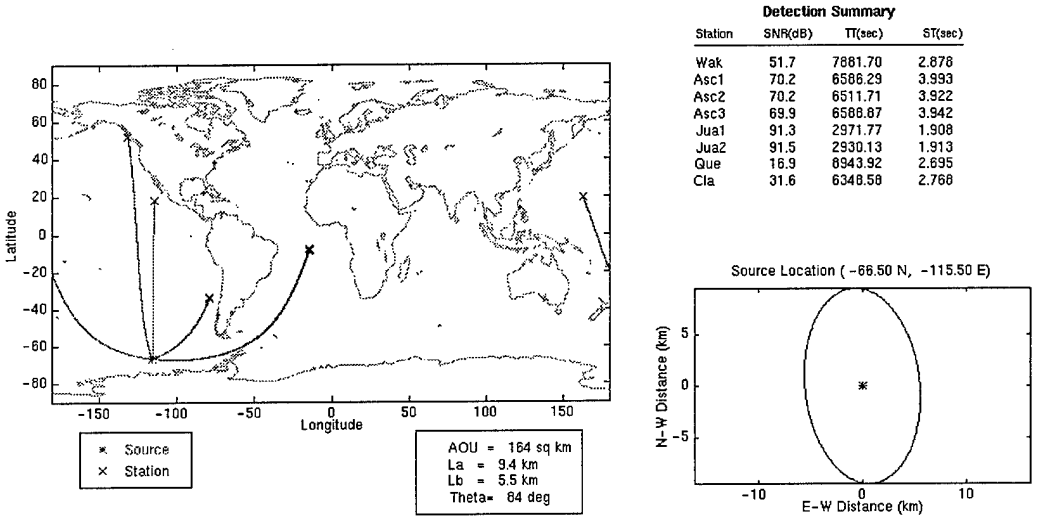

Figure 49: Network performance for a source above the gap

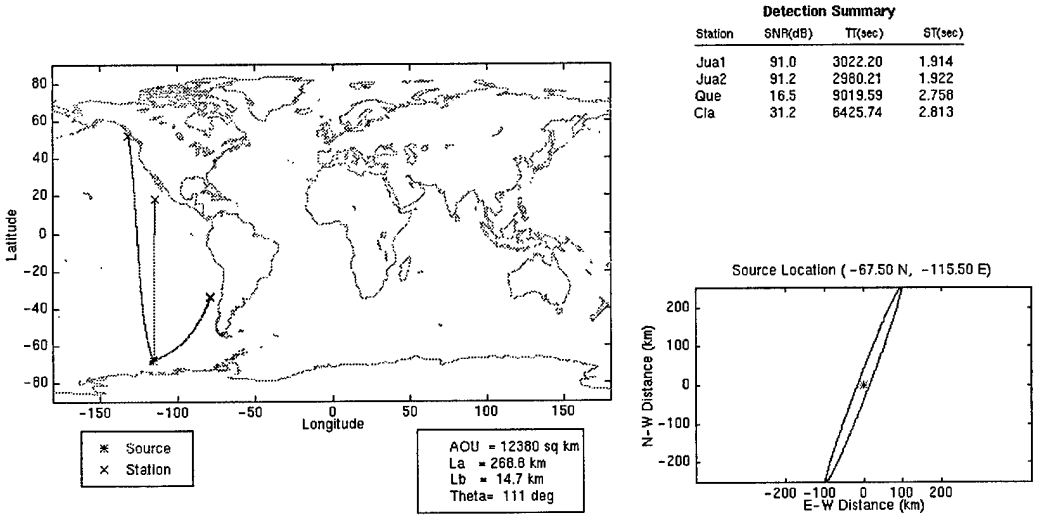

Figure 50: Network performance for a source in the gap

The specific cause of the blockage can be determined by launching a fan of rays from the receiver locations to the vicinity of the source and viewing the bathymetric features along the paths. This process identifies Fiji Island (approx 17°S, 178°E) as the cause of the Wake Island blockage and the South Shetland Islands (between South America and Antarctica) as the cause of the blockage to Ascension Island.

This example shows the ability of HydroCAM to identify the causes of gaps in network coverage. Since high-resolution bathymetric databases and the effects of horizontal refraction are not included, this example is illustrative only.

6.0 Conclusions and Recommendations

A comprehensive, user-friendly model has been developed to predict the ability of acoustic sensors to detect and localizalize nuclear explosions in and above the ocean. Predictions of the model have been compared against measured data. The model has been exercised by BBN and LLNL, and has been used to predict the performance of the IMS and to develop approximate travel time grids for inclusion in the DOE knowledge base. Several studies have been performed to determine the sensitivity of the predictions to the models, interpolation techniques and/or environmental databases used. The following conclusions and recommendations summarize the results of these studies.

6.1 Path Characteristics and Travel Time

Operational hydroacoustic data-processing systems will require accurate predictions of travel times in order to estimate event location. This information is planned to be incorporated into the DOE knowledge base. The data is usually provided in a travel time grid, which contains the predicted travel time from a stationary receiver to a geographic grid of source locations. HydroCAM is the only integrated model capable of resolving the remaining technical issues and generating the required travel time grids. The travel time studies done under this effort have resulting in the following conclusions:

(1) The simplest reasonable propagation model must account for the ellipsoidal nature of the earth and the geographic and seasonal variations in the SOFAR channel sound speed. This model can accurately predict paths and travel times for large expanses of the ocean.

(2) The effects of horizontal refraction are required for cases where paths interact with bathymetric features such as continental shelves, islands and seamounts, and when paths traverse rapidly changing water, such as the Antarctic convergence. However, additional test cases with measured data (that are not antipodal but still include bathymetry and/or changing water temperature) need to be obtained and compared to the model.

(3) The most efficient model for including horizontal refraction will likely use the WKB approximation for the calculation of the acoustic phase velocities, and a boundary value approach to finding refracted rays connecting two points.

(4) Travel time variance can be modeled reasonably well using the historical databases of sound channel fluctuations, and has been benchmarked against one available dataset. Additional data should be used to validate this model, specifically for paths which traverse through high-latitude waters where the variation in sound speed and SOFAR depths is expected to be greatest.

(5) Additional work needs to be done to validate the constant values currently used for characterizing of picking error. This effort will need to include the effects of waveform dispersion and the ability to accurately identify the phases that are being measured.

6.2 Network Performance

HydroCAM is capable of predicting network detection and localization performance including the effects of horizontal refraction and seasonal fluctuations in sound speed. The three major factors affecting network performance are: (1) the specific location of areas blocked by islands and bathymetric features, (2) the actual sensitivity and directionality of the T-Phase stations, and (3) the actual amount of coupling between atmospheric explosions and the SOFAR channel. To address these issues, future efforts should validate the bottom attenuation and horizontal refraction models included in HydroCAM, determine the sensitivity and directionality of the T-Phase stations using measured data, and validate the CALE/NPE treatment of low-atmospheric bursts. Once these issues have been resolved, the HydroCAM has the capability to adjust for these effects.

6.3 Source Effects and Waveform Spectra

The software infrastructure and models are now available to integrate high-fidelity non-linear source models with linear long-range propagation models. However, a number of issues remain in the appropriate use of this capability. The specific areas requiring further investigation are: (1) the artificial effects which are produced due to the mismatch of environmental characteristics (including water depth) used to predict the starter field for the linear model, (2) validation of the starter field and the long-range predicted field with measured data, and (3) the feasibility of predicting a global grid of expected waveform spectral signatures.

6.4 Additional Recommendations

Historical data has shown that reflections from continental shelves and bathymetric features can be observed over long ranges. Other on-going efforts have been investigating the use of these reflections to localize sources from a single sensor. HydroCAM should be upgraded to incorporate reflections. The model can then be used to determine the impact of single-sensor localization algorithms on network performance. HydroCAM

could also be used to determine the sensitivity of the algorithms to database interpolation, sound speed fluctuations and horizontal refraction.

Much of the software infrastructure in HydroCAM is applicable to the infrasound monitoring technology. A short feasibility study should be performed to determine the need and level of effort necessary to add existing environmental databases and models for the detailed prediction of infrasound network performance. An integrated model would support joint hydroacoustic-infrasound detection and localization studies.

7.0 References

[1] T.R Farrell, K.D LePage, C.B. Barclay. *Users Guide for the Hydroacoustic Coverage Assessment Model (HydroCAM).* BBN Technical Report W1273, August 1996.

[2] T.R. Farrell and K.D. LePage. *Travel time variability and localization accuracy for global scale monitoring of underwater acoustic events.* JASA **99**(4), April 1996.

[3] K.D. LePage and T.R. Farrell. *The effect of sound speed fluctuations on travel time variability and localization accuracy of global hydrophone networks.* To be submitted to JASA, September 1996.

[4] D.B. Clarke, *Pressure Time Histories Derived from Hydroacoustic Coupling Calculations: The Transition to Long Range Linear Acoustics.* LLNL Report UCRL-ID-122595, December 1995.

[5] J. Wakeley, *Pressure Signature Model for an Underwater Explosive Charge,* US Navy Journal of Underwater Acoustics Vol 27, No2. April 1977.

[6] G.M. Wenz, *Acoustic Ambient Noise in the Ocean, Spectra and Sources.* JASA **34**(12), December 1962.

[7] D.B. Harris (LLNL), Personal Communication.

[8] K.D. Heaney, W.A. Kuperman and B.E McDonald. "Perth-Bermuda sound propagation (1960): Adiabatic mode interpretation", JASA **90**(5), November 1991, p. 2589.

[9] R.M. Jones, J.P. Riley, and T.M. Georges, *HARPO: A Versatile Three-Dimensional Hamiltonian Ray-Tracing Program for Acoustic Waves in an Ocean with Irregular Bottom.* NOAA Wave Propagation Laboratory, October 1986.

[10] W. H. Munk, W. C. O'Reilly, and J.L. Reid. *Australia-Bermuda Sound Transmission Experiment (1960) Revisited,* J. Phys. Oceanol. **18**, 1876 (1988).

[11] M. D. Collins and W. A. Kuperman, *Overcoming ray chaos,* JASA **95**, p 3167-3170 (1994)

[12] W. H. Press, B. P. Flannery, S. A. Teukolsky and W. T. Vetterling, Numerical Recipes in C, Cambridge University Press, Cambridge 1988, p. 609-621.

[13] [Hydrographic Atlas of the Southern Oceans, Alfred Wegener Institute, http://www.awi-bremerhaven.de/, 1995.

[14] R. J. Urick, Principles of Underwater Sound, McGraw Hill, New York (1983), Chap. 5

[15] JASA **96** (4), October 1994. This issue contains a collection of papers describing the Heard Island Feasibility Test (HIFT).

[16] R.C. Shockley, J. Northrop and P.G. Hansen. *SOFAR Propagation Paths from Australia to Bermuda: Comparison of Signal Speed Algorithms and Experiments*, JASA **71**(1) p. 51, January 1982.

[17] K. Mackenzie, "Nine-term Equation for Sound Speed in the Oceans", JASA **70**, p. 807, 1981.

[18] D.R. Palmer, T.M. Georges, J.J. Wilson, L.D. Weiner, J.A. Paisley, R. Mathiesen, R.R. Pleshek and R.R. Mabe. "Reception at Ascension of the Heard Island Feasibility Test Transmissions", JASA **96** (4), October 1994.

[19] E. Scheer (WHOI), Personal Communication.

[20] *Report of the Expert Group based on Technical Discussions held from 4 through 15 December 1995, Working Group 1 - Verification*, Conference on Disarmament Paper CD/NTB/WP.283, 20 December 1995.

[21] G. I. Evenden. *Cartographic Projection Procedures for the UNIX Environment -- A Users Manual,* USGS Open-File Report 90-284, August 1991.

8.0 Acronyms

AFTAC	Air Force Technical Applications Center
AOU	Area of Uncertainty
ASW	Anti-Submarine Warfare
CTBT	Comprehensive Test Ban Treaty
DOE	Department of Energy
ESL	Energy Source Level
FD	Finite Differences
GDEM	Generalized Digital Environmental Model
HARPO	Hamiltonian Acoustic Raytrace Program for the Ocean
HR	Horizontal Refraction
HydroCAM	Hydroacoustic Coverage Assessment Model
IMS	International Monitoring System
IVSEM	Integrated Verification System Evaluation Model
JASA	Journal of the Acoustical Society of America
LLNL	Lawrence Livermore National Laboratory
NJIT	New Jersey Institute of Technology
NOAA	National Oceanographic and Atmospheric Administration
NPE	Non-linear Parabolic Equation
NRL	Naval Research Laboratory
RAM	Range-dependent Acoustic Model
SNL	Sandia National Laboratory
SNR	Signal to Noise Ratio
SOFAR	Sound Fixing and Ranging
SONAR	Sound Navigation and Ranging
TL	Transmission Loss
USGS	United States Geologic Survey
WHOI	Woods Hole Oceanographic Institution
WKB	Wenzel-Kramers-Brillouin
WOA	World Ocean Atlas

RALPH ALEWINE
NTPO
1901 N. MOORE STREET, SUITE 609
ARLINGTON, VA 22209

LT CMDR ROBIN L. ATKINS
N874/D
2000 NAVY PENTAGON, RM 5D580
WASHINGTON, DC 20350-2000

RICHARD BARDZELL
ACIS
DCI/ACIS
WASHINGTON, DC 20505

GERALD S. BARTON
NOAA
1825 CONNECTICUT AVE. NW
WASHINGTON, DC 20235

RICHARD C. BECKMAN
SANDIA NATIONAL LABORATORY
DEPT. 5791
MS 0567, PO BOX 5800
ALBUQUERQUE, NM 87185-0567

ROBERT BLANDFORD
AFTAC/CMR
1300 N. 17TH STREET
SUITE 1450
ARLINGTON, VA 22209-2308

STEVEN BRATT
NTPO
1901 N. MOORE STREET, SUITE 609
ARLINGTON, VA 22209

LESLIE A. CASEY
HQ DOE
1000 INDEPENDENCE AVE. SW
NN-20
WASHINGTON, DC 20585-0420

ALBERT J. CHABAI
SANDIA NATIONAL LABORATORY
DEPT. 9311
MS 1159, PO BOX 5800
ALBUQUERQUE, NM 87185-1159

ERIC P. CHAEL
SANDIA NATIONAL LABORATORY
DEPT. 9311
MS 1159, PO BOX 5800
ALBUQUERQUE, NM 87185-1159

JOHN P. CLAASSEN
SANDIA NATIONAL LABORATORY
DEPT. 5736
MS 0655, PO BOX 5800
ALBUQUERQUE, NM 87185-0655

DOUG CLARKE
LAWRENCE LIVERMORE NATIONAL
LABORATORY
PO BOX 808, MS L-200
LIVERMORE, CA 94551

DENNIS M. CONLON
SPAWAR
PMW 1820C 2451 CRYSTAL DRIVE
ARLINGTON, VA 22245-5200

ROBERT H. CORBELL
SANDIA NATIONAL LABORATORY
DEPT. 5736
MS 0655, PO BOX 5800
ALBUQUERQUE, NM 87185-0655

CWO LESLIE CRAIG
OSIA
300 W. SERVICE ROAD, DULLES
PO BOX 17498
WASHINGTON, DC 20041-0498

RON CUMMINGS
C & A
3941 SOUTH BRISTOL STREET
SUITE 317
SANTA ANA, CA 92704

MARVIN D. DENNY
LAWRENCE LIVERMORE NATIONAL
LABORATORY
PO BOX 808, MS L-205
LIVERMORE, CA 94551

DR. STANLEY DICKINSON
AFOSR
110 DUNCAN AVENUE
SUITE B115
BOLLING AFB, WASHINGTON D.C. 20332-001

SEAN DORAN
ACIS
DCI/ACIS
WASHINGTON , DC 20505

MICHAEL W. EDENBURN
SANDIA NATIONAL LABORATORY
DEPT. 4115
MS 0329, PO BOX 5800
ALBUQUERQUE, NM 87185-0329

JOHN FILSON
ACIS/TMG/NTT
ROOM 6T11 NHB
WASHINGTON, DC 20505

FREDERICK E. FOLLOWILL
LAWRENCE LIVERMORE NATIONAL
LABORATORY
PO BOX 808, MS L-208
LIVERMORE, CA 94551

RADM (RET) THOMAS FOX
PACIFIC NORTHWEST NATIONAL
LABORATORY
PO BOX 999, MS K6-48
RICHLAND, WA 99352

DAN N. HAGEDORN
PACIFIC NORTHWEST NATIONAL
LABORATORY
PO BOX 999, MS K7-34
RICHLAND, WA 99352

WILLARD J. HANNON JR.
LAWRENCE LIVERMORE NATIONAL
LABORATORY
PO BOX 808, MS L-205
LIVERMORE, CA 94551

TERRI HAUK
LAWRENCE LIVERMORE NATIONAL
LABORATORY
PO BOX 808, MS L-205
LIVERMORE, CA 94551

W. MARK HODGSON
LOS ALAMOS NATIONAL LABORATORY
PO BOX 1663 MS D460
LOS ALAMOS, NM 87545

ED MCDONALD
NAVAL RESEARCH LABORATORY
4555 OVERLOOK AVE. SW
WASHINGTON, DC 20375-5350

LARRY NG
LAWRENCE LIVERMORE NATIONAL
LABORATORY
PO BOX 808, MS L-285
LIVERMORE, CA 94551

CLYDE E. NISHIMURA
NAVAL RESEARCH LABORATORY
4555 OVERLOOK AVE. SW
WASHINGTON
DC, 20375-5350

GEORGE V. FISK
WOODS HOLE OCEANOGRAPHIC INSTITUTION
OCEANOGRAPHIC INSTITUTION
APPLIED OCEAN PHYSICS &ENGINEERING
BIGELOW 107B
WOODS HOLE, MA 02543

CHRIS FOX
NOAA
2115 SE OSU DRIVE
NEWPORT, OR 97364

CDR MARTHA GILLETTE
N514F
2000 NAVY PENTAGON, RM 4D563

RICHARD C. HANLEN
PACIFIC NORTHWEST NATIONAL
LABORATORY
PO BOX 999, MS K6-40
RICHLAND, WA 99352

DAVID B. HARRIS
LAWRENCE LIVERMORE NATIONAL
LABORATORY
PO BOX 808, MS L-205
LIVERMORE, CA 94551

PRESTON B. HERRINGTON
SANDIA NATIONAL LABORATORY
DEPT. 5736
MS 0655, PO BOX 5800
ALBUQUERQUE, NM 87185-0655

LESTER MACHTA
NOAA
1825 CONNECTICUT AVE. NW
WASHINGTON, DC 20235

ED NAWROCKI
OSD
OSD/ISP/NSS
WASHINGTON, DC 20301-2600

WESLEY L. NICHOLSON
PACIFIC NORTHWEST NATIONAL
LABORATORY
PO BOX 999, MS K6-40
RICHLAND, WA 99352

MARSHALL H. ORR
NAVAL RESEARCH LABORATORY
4555 OVERLOOK AVE. SW
WASHINGTON
DC, 20375-5350

GREGORY ORRIS
NAVAL RESEARCH LABORATORY
4555 OVERLOOK AVE. SW
WASHINGTON
DC, 20375-5350

DOUGLAS REVELLE
LOS ALAMOS NATIONAL LABORATORY
PO BOX 1663, MS F665
LOS ALAMOS, NM 87545

RICK SCHULT
HQ/AFTAC/TTR
1030 S. HIGHWAY A1A
PATRICK AFB, FL 32925-3002

DAVID J. SIMONS
LOS ALAMOS NATIONAL LABORATORY
PO BOX 1663, MS D460
LOS ALAMOS, NM 87545

ROBERT SPINDEL
UNIVERSITY OF WASHINGTON
1013 NE 40TH STREET
SEATTLE, WA 98105-6698

STEVEN R. TAYLOR
LOS ALAMOS NATIONAL LABORATORY
PO BOX1663, MS C335
LOS ALAMOS, NM 87545

LAWRENCE TURNBULL
ACIS
DCI/ACIS
WASHINGTON, DC 20505

THOMAS A. WEAVER
LOS ALAMOS NATIONAL LABORATORY
PO BOX 1663 MS C335
LOS ALAMOS, NM 87545

CAPT. HAROLD WILLIAMS
SPAWAR
PD-80, 2451 CRYSTAL DRIVE
ARLINGTON, VA 22245-5200

OFFICE OF THE SECRETARY OF DEFENSE
DDR&E
WASHINGTON, DC 20330

FRANK PILOTTE
HQ/AFTAC/TT
1030 S. HIGHWAY A1A
PATRICK AFB, FL 32925-3002

JUDY SCHROEDER
OSIA
300 W. SERVICE ROAD, DULLES
PO BOX 17498
WASHINGTON, DC 20041-0498

JOSEPH SCHRODT
HQ/AFTAC/TTR
1030 S. HIGHWAY A1A
PATRICK AFB, FL 32925-3002

JOHN SPIESBERGER
PENN STATE UNIVERSITY
512 WALKER BLDG.
UNIVERSITY PARK, PA 16802

BRIAN W. STUMP
LOS ALAMOS NATIONAL LABORATORY
PO BOX 1663, MS C335
LOS ALAMOS, NM 87545

LAWRENCE TROST
SANDIA NATIONAL LABORATORY
DEPT. 4115
MS 00329, PO BOX 5800
ALBUQUERQUE, NM 87185-0329

LARRY S. WALKER
SANDIA NATIONAL LABORATORY
DEPT. 5704
MS 0979, PO BOX 5800
ALBUQUERQUE, NM 87185-0979

JOHN W. WHITE
LAWRENCE LIVERMORE NATIONAL
LABORATORY
PO BOX 808, MS L-200
LIVERMORE, CA 94551

JOHN ZUCCA
LAWRENCE LIVERMORE NATIONAL
LABORATORY
PO BOX 808, MS L-205
LIVERMORE, CA 94551

DEFENSE TECHNICAL INFORMATION CENTER
8725 JOHN J. KINGMAN ROAD
FT BELVOIR, VA 22060-6218 (2 COPIES)

TACTEC
BATTELLE MEMORIAL INSTITUTE
505 KING AVENUE
COLUMBUS, OH 43201 (FINAL REPORT)

PHILLIPS LABORATORY
ATTN: GPE
29 RANDOLPH ROAD
HANSCOM AFB, MA 01731-3010

PHILLIPS LABORATORY
ATTN: PL/SUL
3550 ABERDEEN AVE SE
KIRTLAND, NM 87117-5776 (2 COPIES)

THEODORE R. FARRELL
BBN SYSTEMS & TECHNOLOGIES
1300 NORTH 17TH STREET
SUITE 1200
ARLINGTON, VA 22209

PHILLIPS LABORATORY
ATTN: XPG
29 RANDOLPH ROAD
HANSCOM AFB, MA 01731-3010

PHILLIPS LABORATORY
ATTN: TSML
5 WRIGHT STREET
HANSCOM AFB, MA 01731-3004

CATHERINE DEGROOT-HEDLIN
UNIVERSITY OF CA, SAN DIEGO
SCRIPPS INSTITUTION OF OCEANOGRAPHY,
IGPP, 0225
9500 GILMAN DRIVE
LA JOLLA, CA 92093-0225

JOHN A. ORCUTT
UNIVERSITY OF CA, SAN DIEGO
SCRIPPS INSTITUTION OF OCEANOGRAPHY,
IGPP, 0225
9500 GILMAN DRIVE
LA JOLLA, CA 92093-0225